Chem Soc Rev

REVIEW ARTICLE

View Article Online
View Journal | View Issue

Cite this: *Chem. Soc. Rev.*, 2017, **46**, 102

In situ X-ray absorption spectroscopy of transition metal based water oxidation catalysts

Christina H. M. van Oversteeg,[a] Hoang Q. Doan,[b] Frank M. F. de Groot*[a] and Tanja Cuk*[b]

Received 19th March 2016

DOI: 10.1039/c6cs00230g

www.rsc.org/chemsocrev

X-ray absorption studies of the geometric and electronic structure of primarily heterogeneous Co, Ni, and Mn based water oxidation catalysts are reviewed. The X-ray absorption near edge and extended X-ray absorption fine structure studies of the metal K-edge, characterize the metal oxidation state, metal–oxygen bond distance, metal–metal distance, and degree of disorder of the catalysts. These properties guide the coordination environment of the transition metal oxide radical that localizes surface holes and is required to oxidize water. The catalysts are investigated both as-prepared, in their native state, and under reaction conditions, while transition metal oxide radicals are generated. The findings of many experiments are summarized in tables. The advantages of future X-ray experiments on water oxidation catalysts, which include the limited data available of the oxygen K-edge, metal L-edge, and resonant inelastic X-ray scattering, are discussed.

1 Introduction

The increase in world population together with an increase in living standards is causing an increase in energy consumption.[1,2] Currently fossil fuels are by far the most important natural energy resource. However, these reserves are finite and the combustion of fossil fuels has significant negative effects on the environment. As a consequence, there is an urgent need for inexhaustible, renewable and clean energy sources.

Artificial photosynthetic systems that harness solar energy by converting it into a storable carbon-free fuel are poised to replace fossil fuels. In artificial photosynthetic systems, water is an essential fuel feedstock: it is both abundant and uniquely provides for a highly selective, uphill reaction. The water splitting process can be broken down into two steps, the oxygen evolution reaction (OER) to produce O_2, protons and electrons ($2H_2O \rightarrow 4H^+ + 4e^- + O_2$), followed by the reduction of protons

Christina H. M. van Oversteeg

Christina van Oversteeg received her MSc degree in Chemistry from Utrecht University in 2015. The research for her MSc thesis focused on the use of XAS for investigating the structure of conventional HDS catalysts and was supervised by Frank de Groot. An additional research project was carried out at UC Berkeley under the supervision of Tanja Cuk. Currently, she is working as a PhD student at Utrecht University in the Netherlands. Her research focuses on the photocatalytic properties of copper chalcogenide nanocrystals.

Hoang Q. Doan

Hoang Q. Doan received a BS in chemistry from Purdue University in 2010. Her undergraduate research with Joseph Francisco was on bio-computational modeling of radical attack on amide systems to mimic small sections of protein misfolding. She obtained her PhD in chemistry in 2016 from the University of California, Berkeley working with Tanja Cuk on the photo-dynamics of oxygen-evolving semiconductors using ultrafast transient spectroscopy.

---

[a] *Department of Chemistry, Utrecht University, Universiteitsweg 99, 3584 CG Utrecht, The Netherlands. E-mail: F.M.F.deGroot@uu.nl*
[b] *Department of Chemistry, University of California – Berkeley, 419 Latimer Hall, Berkeley, CA 94720, USA. E-mail: Tanjacuk@berkeley.edu*

to form H_2 ($2H^+ + 2e^- \rightarrow H_2$). Due to the four electron transfers required, the OER is especially demanding, and catalysts to increase the rate of the reaction have been investigated for decades.[3] Transition metal oxide materials, whose surfaces are easily hydroxylated, have proven to be among the best water oxidation catalysts (WOCs).[4] The metric for their catalytic properties is the O_2 evolution rate at a particular over-potential. The over-potential is defined as the difference between the applied potential and the thermodynamic potential for water oxidation (1.23 V *vs.* SHE, pH = 0). As an example, the O_2 evolution rate per site is in the range of 0.01–0.1 O_2/Co site for Co_3O_4 with a moderate over-potential of 0.3–0.4 V.[5] The over-potential can be tuned either by a voltage in an electrochemical cell or by photo-excitation. Both an applied voltage and photo-excitation provide positive charges, or holes, that then accept electrons from water; while a voltage can continuously tune the potential of holes, photo-excitation (either by charge transfer from a light-absorbing dye molecule or by exciting the catalyst itself) leads to holes at the potential defined by the lowest occupied band in the material, *i.e.* the valence band.

Fundamental descriptions of the catalytic activity of transition metal oxide materials start with the ground state atomic and electronic structure. This ground state structure is defined by the catalyst surface at equilibrium with a given pH. The catalyst could be at an applied potential below the thermodynamic potential of the reaction. For the purposes of this review, we define this to be the as-prepared structure of the catalyst. The as-prepared structure important to catalysis is guided by the local, molecular properties: the hybridization between the metal and the oxygen site, the oxidation state of the metal, the metal–oxygen distance, structural distortions and the degree of disorder. All of these electronic properties guides the coordination environment of a localized hole at a surface site from which a catalytic reaction can proceed. X-ray absorption spectroscopy (XAS) is a unique tool to investigate these local properties, because it excites an electron from core levels (1s, 2p of the metal and 1s of the oxygen) to an unoccupied band (metal 2p, 3d and oxygen 2p) and therefore is element specific. Further, extended X-ray absorption spectroscopy (EXAFS) determines bond distances and short-range order from the recoil of the atoms around the excited one. The first part of this review covers the XAS obtained ground state atomic and electronic properties of as-prepared transition metal oxide catalysts. The hard X-ray metal K-edge (1s to 2p transition) features prominently, due to the extensive work in this area; the more recent studies of the soft X-ray oxygen K-edge and metal L-edge (2p to 3d transition) are highlighted as well.

An even better probe of the coordination environment of a localized surface hole is to investigate these catalysts under reaction conditions with XAS and EXAFS. These reaction conditions are obtained in custom made cells that allow for the X-ray beam to penetrate the electrode through to the catalyst/electrolyte interface. Recent techniques include the development of liquid cells for use in an ultra-high vacuum chamber and flow cells that allow for electrolyte and gas circulation.[6] In these experiments, one observes changes to the average oxidation state, metal–oxygen distance, structural distortions, and the degree of disorder in the material due to catalysis. Due to the fact that XAS is bulk sensitive, the effect of holes accumulating in the bulk and at the catalytic surface will be measured. Further, during catalysis, holes will both localize at the surface and transfer to the electrolyte, which could lead to small net changes with respect to the as-prepared catalyst. On the other hand, many of the heterogeneous catalysts investigated are generated electrochemically, which means that in the as-prepared state, they are porous and contain a large surface area.[7] Furthermore, recent infrared experiments of WOCs under illumination,[8] transient optical spectroscopy on the millisecond time-scale,[9] and photoelectrochemical measurements[10] suggest that under a steady state reaction, holes will accumulate at the surface. Therefore, if the average metal oxidation state increases as determined by metal K-edge XAS, it suggests that a surface

Frank M. F. de Groot

Dr de Groot received his MSc degree in Chemistry from Nijmegen University in 1986 and a PhD in Chemistry from Nijmegen University in 1991. He then went on to the LURE synchrotron in Orsay, France, from 1992 to 1994 and to a KNAW academy researcher position at Groningen University from 1995 to 1998. Since 1999, he has been working in the Chemistry Department of Utrecht University, since 2009 as professor in X-ray spectroscopy. His research is focused on X-ray spectroscopy for the study of the electronic and magnetic structure of condensed matter, in particular for transition metal oxides and heterogeneous catalysts under working conditions.

Tanja Cuk

Dr Cuk finished a BSE in Electrical Engineering at Princeton University in 2000 and a PhD in Applied Physics at Stanford University in 2007. She then went on to a Miller Postdoctoral Fellowship at UC Berkeley from 2007 to 2010. Since 2010, she has been an Assistant Professor in the Chemistry Department at UC Berkeley and a Faculty Scientist within the Chemical Sciences Division at Lawrence Berkeley National Laboratory. Her research aims to elucidate solar-to-fuel generation and focuses on the fundamental mechanisms involved in converting charge into fuel at solid–liquid interfaces, for which she applies multiple ultrafast spectroscopy.

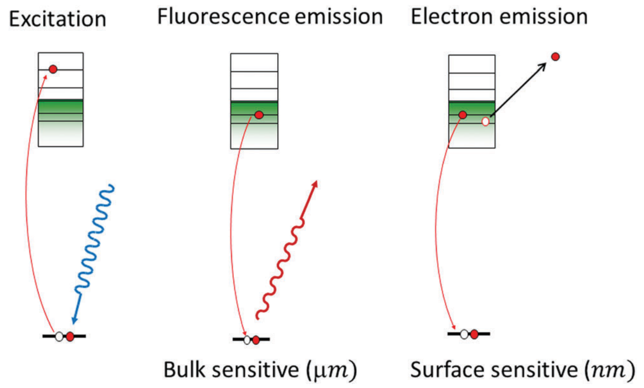

Fig. 1 The XAS measurements depicting the initial X-ray excitation to unoccupied electronic states (left), the fluorescent X-ray probe of the emissive transition of occupied electronic states filling the core hole (middle), and the electron yield probe that results from emitted electrons (right).

hole has substantial metal character, and has less tendency to localize on surface oxygen sites. The second part of this review covers the XAS/EXAFS obtained atomic and electronic structure of transition metal oxide catalysts under reaction conditions. Here, almost exclusively the metal K-edge is investigated, although techniques are becoming available for *in situ* soft X-ray studies.[6,11]

The spectrum that XAS probes is diagramed in Fig. 1. In general, the X-ray fluorescence from the catalyst is collected as a function of the incident X-ray energy. The X-ray energy tunes the excitation of core-level electrons to different, unoccupied electronic states (left), which modulates the intensity of fluorescent, electronic transitions of electrons in the occupied valence states to the unoccupied core levels (middle). Another way to obtain a spectrum as a function of X-ray energy is to collect the total electron yield, or the current between two contacts that is induced by the incident X-rays. The electron yield is considered especially surface sensitive (1–2 nm) since it is generated by low energy electrons emitted from the sample (right). With fluorescence or electron yield, a spectrum of the unoccupied electronic structure of either the as-prepared catalyst or the catalyst under reaction conditions is obtained.

The focus of this XAS/EXAFS review is the OER activity of heterogeneous, oxide catalysts containing cobalt (Co), nickel (Ni), and manganese (Mn). Oxides of these three metals are promising and affordable materials for water oxidation.[12–14] CoO-, NiO- and MnO-based electrocatalysts generally operate at lower over-potentials than transition metal oxides such as Fe_2O_3 and TiO_2.[15,16] Co, Ni, and Mn oxides are also differentiated by being essentially "dark" catalysts, such that only a voltage or a separate light absorber can inject holes into the ground state electronic structure and generate appreciable catalytic activity. The low over-potential has previously been attributed to the ability of these catalysts to transition between different oxidation states, *i.e.* the presence of multiple redox potentials, and the metal–oxygen bond strength.[17,18] Suggested OER schemes for CoO- and MnO-based catalysts predict that a hole localizes preferentially on the metal site, creating surface metal oxos (M=O) in converting Co/Mn(III)OH–Co/Mn(III)OH to Co/Mn(IV)OCo/Mn(IV)O. For NiO-based catalysts, OER schemes predict that the hole localizes on an oxygen atom, creating anoxyl radical, Ni(III)–O•.[19–22] The transition metal oxide radical generated by surface hole localization, however, could be a delicate balance of the oxidation state of the metal and the oxygen. In addition to the XAS studies reviewed below, recent efforts have reported on such radicals based on their vibrational spectrum in steady state and time-resolved infrared experiments, notably the Co(IV)=O radical of Co_3O_4,[8] the Ti–O• radical of $SrTiO_3$[23] and the Fe(IV)=O radical of Fe_2O_3.[24] Observation of the direct spin density distribution of a radical was reported for a Ru=O fragment in a molecular WOC by electron paramagnetic resonance.[25]

The nature of this radical is expected to determine a transition metal oxide catalyst's ability to promote the formation of the O–O bond. In the proposed water oxidation cycle depicted in Fig. 2, two transition metal oxide radicals are involved in oxidizing a water molecule into the O–O bond, thought to be the rate limiting step of the water oxidation reaction.[3] There are

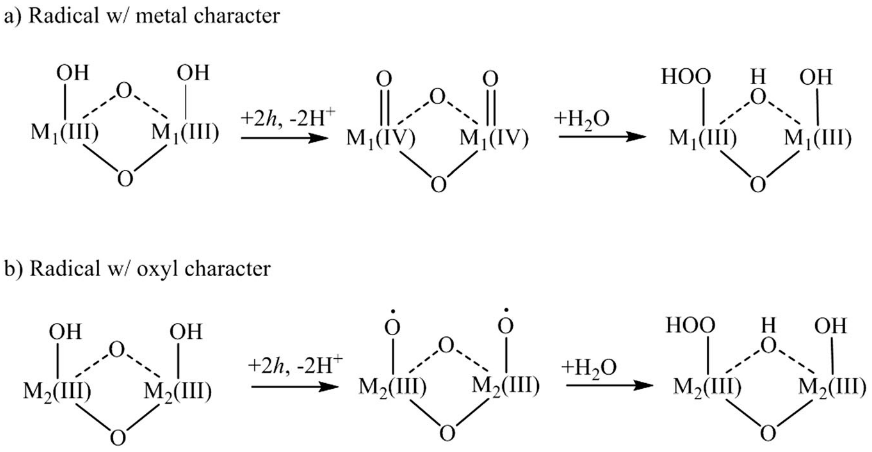

Fig. 2 Catalytic mechanism depicting (a) a transition metal oxide radical with metal character generated by hole injection and (b) a transition metal oxide radical with oxyl character generated by hole injection.

two proposed routes for generating O_2 from the as-prepared catalyst at equilibrium, adapted from previously proposed mechanisms for Co, Mn catalysts[22] (Fig. 2a) and Ni catalysts[20] (Fig. 2b). The first highlights the role of the transition metal oxide radical with metal character: two hole transfers generate two metal oxos that then nucleophilically attack water to create O_2. The second highlights the transition metal oxide radical with oxygen character: here, two hole transfers create two oxyl radicals that then nucleophilically attack water. While there are other mechanism that could describe O–O bond formation, the initial transition metal oxide radical supported by the as-prepared catalyst will be a defining characteristic in any given one. The atomic and electronic information on the transition metal oxide radical can be provided for by comparing XAS and EXAFS of as-prepared catalysts with that of catalysts under reaction conditions.

The review is divided into the following sections: (2) theory of XAS and EXAFS. The theory section primarily concerns the metal K-edge, metal L-edge, and O K-edge XAS/EXAFS, but also includes a brief description of resonant inelastic X-ray absorption scattering (RIXS) useful for future studies. (3) *Ex situ* metal K,L-edge XAS. This section reviews the results on as-prepared WOCs. (4) *In situ* metal K-edge XAS. This section reviews the results on WOCs under reaction conditions. The experimental sections (3) and (4) include an overview of the results of many XAS experiments in a tabular form. Comparisons between the *ex situ* and *in situ* tables are made. (5) Soft X-ray absorption of WOCs. This section discusses the recent cell development involved in the application of soft X-ray and RIXS to investigating catalysis, the limited studies currently available, and how the broader application of these techniques to catalysis could impact the field. For further reading, the reader is referred to several other reviews on X-ray spectroscopy[26–29] and WOC.[1,2,30–33]

2 X-ray absorption spectroscopy

When an X-ray passes an electron, the electron can capture energy as the X-ray causes the field to oscillate in both strength and direction. If the energy gain by the electron is equal to or higher than the binding energy of the core electron, a photon can be absorbed. A core electron is then excited to an excitonic state below the ionization threshold or to a free electron with a certain kinetic energy above the ionization threshold, as illustrated in Fig. 3.

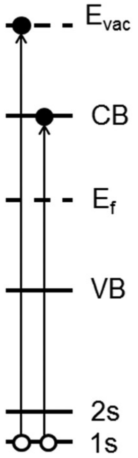

Fig. 3 XAS energy diagram, where the left part depicts the excitation of a core electron to an excitonic state below the ionization threshold and to a free electron with a certain energy above the ionization threshold.

The Fermi golden rule gives the transition probability W_{fi} between the initial (ϕ_i) and the final state (ϕ_f) of the absorption process:

$$W_{fi} = \frac{2\pi}{\hbar}|\langle\phi_f|T|\phi_i\rangle|^2\delta_{E_f-E_i-\hbar\omega} \tag{1}$$

Conservation of energy is included by the delta function, δ, with E_f the final state energy, E_i the initial state energy and $\hbar\omega$ the energy of the incident photon. The transition operator T is related to the interaction Hamiltonian and contains the term e^{ikr}, with k as the wave vector of the X-rays. According to the Taylor expansion, the term e^{ikr} can be written as $1 + ikr + \cdots$. Since the wavelength of an X-ray photon is much larger than the typical size of an atom, the factor kr is $\ll 1$. Consequently, the dipole approximation can be used, which turns the transition operator into the dipole operator, r, and the Fermi golden rule can be written as

$$W_{fi} \propto |\langle\phi_f|r|\phi_i\rangle|^2\delta_{E_f-E_i-\hbar\omega} \tag{2}$$

For excitations from the 1s core states the interactions between electrons in the final state are relatively weak and a single electron excitation approximation can be employed. In this case the initial state can be written as a core wave function (c) and the final state as a valence electron wave function (ε). The squared matrix element M is assumed constant as it only has a small variation in energy. Subsequently the Fermi golden rule can be rewritten as

$$|\langle\phi_f|r|\phi_i\rangle|^2 = |\langle\varepsilon|r|c\rangle|^2 = M^2 \tag{3}$$

$$I_{XAS} \sim M^2\rho \tag{4}$$

The delta function in the Fermi golden rule suggests that the absorption spectrum should look like the density of unoccupied states, broadened by the lifetime broadening as discussed below.

Variations in the X-ray absorption coefficient μ are measured as a function of the incident X-ray energy. At a certain incoming photon energy a sharp rise in absorption will occur, referred to as the absorption edge or main edge. At this specific energy, the photon energy is equal to the binding energy of a specific core level. The K-edge relates to the transitions of the 1s core electron to the 4p conduction band, whereas the L-edge relates to transitions of the 2s and 2p core electrons to the 3d band. The excitation of a core electron results in an unstable state due to the presence of a core hole. The core hole will be filled by decay processes such as fluorescence or Auger.

The absorption spectrum can be roughly divided into two regions (Fig. 4). The region at energies below and around the ionization threshold is referred to as the X-ray absorption near edge structure (XANES). Around 20 to 30 eV above the

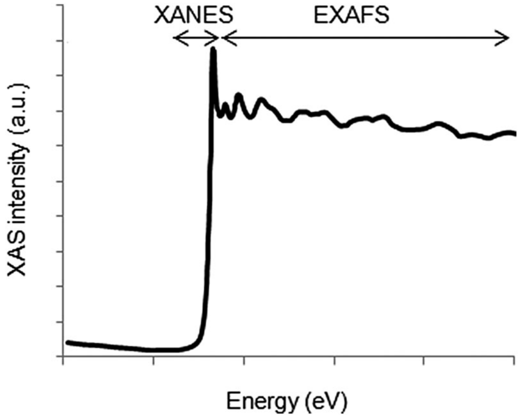

Fig. 4 The X-ray absorption spectrum can be divided into the XANES region, describing the edge structure up to around 25 eV above the edge, and the EXAFS region at higher energies.

absorption edge, the excited electron is typically described using the electron scattering description and this region is referred to as the extended X-ray absorption fine structure (EXAFS). The two regions are further discussed below in terms of the information they provide.

2.1 Typical K-edge XANES for 3d metal oxides

For 3d transition metals, the K-edge is found in the hard X-ray regime (5–10 keV). The main absorption edge corresponds to transitions from the 1s to 4p states, while the corresponding pre-edge covers transitions from the 1s to 3d states. A typical K-edge spectrum for a 3d metal is given in Fig. 5.

In order for a transition to be allowed, the matrix element should be non-zero. Consequently two selection rules should be obeyed. The first selection rule states that the orbital quantum number of the final state can only differ by one from the initial state ($\Delta L = +1$ or -1) as light carries an orbital momentum of one. According to this selection rule a transition from an s orbital will be into a p orbital, *i.e.* from $l = 0$ to $l = 1$. The main quantum number does not have a selection rule. Therefore both 1s2p and 2s2p transitions are allowed. The second selection rule is the spin selection rule, which states that the spin of an electron cannot be modified during interaction with light as light does not carry spin ($\Delta S = 0$).

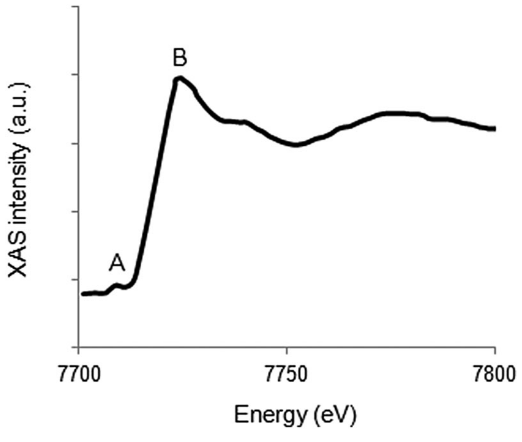

Fig. 5 Representation of the Co K-edge XAS structure. The pre-edge is marked by A, whereas B indicates the main absorption edge.

There is much chemical information present in the XANES region. In the case of bulk oxides, the position of the edge is sensitive to the formal oxidation state of the element. This can be explained by an increase in the electrostatic interaction between the positive metal ion and negative electrons, caused by a decrease in the shielding of charge by the absence of extra electronic charge or higher oxidation states.[34] Wong *et al.* (1984) found that for bulk metal oxides, the edge energy is linearly related to the formal oxidation state with a slope of $\sim$2 eV per valence.[35] For clarity we note that this concept of the X-ray absorption edge is not directly related to the ionization potential, but serves as an empirically determined parameter that correlates with the formal valence of the system. Three common methods to determine the edge position are (1) the energy at 50% intensity of the edge maximum, (2) averaging energies at 20% and 80% intensity of the edge maximum and (3) the energy of the inflection point.[36] If the edge is more than a single feature, for example containing a shoulder, different methods may report different edge energies. Therefore, consistency in the chosen method is important to properly relate edge energies to the formal oxidation state. The spectral shape and absorption edge position are also sensitive to ligand types and the coordination environment.

The pre-edge feature in K-edge XAS gives important electronic and structural information. We discuss a number of limiting cases as examples: (a) in the case of isolated octahedral transition metal ions, the pre-edge corresponds to the 1s3d quadrupole transition, where the pre-edge is split by the crystal field effect into t_{2g} and e_g peaks. (b) If inversion symmetry is broken such as in tetrahedral symmetry, there is hybridization of the 3d and 4p orbitals, implying that there are also direct dipole transitions into the pre-edge region strongly enhancing the pre-edge intensity. From the symmetry argument one can deduce that only the t_2-symmetry states have dipole–quadrupole mixing. This implies that intense pre-edge features are indicative of a geometry distortion from a centrosymmetric environment.[37] (c) In the case of bulk oxides without inversion symmetry the situation is similar to an isolated complex, but in a bulk system with inversion symmetry, there are two separate pre-edge structures: (c1) the usual 1s3d quadrupole pre-edge and (c2) the 1s4p dipole pre-edge that is due to transitions of 4p states that hybridize with the 3d states of near neighbors. The energy splitting between these two types of pre-edges is typically 2.5 eV.[38] Besides symmetry information, the pre-edge also contains information on the formal metal oxidation state. For bulk oxides, the pre-edge energy is linearly related to the formal oxidation state.[35]

2.2 Metal K-edge EXAFS

At the EXAFS energies, electrons are excited into the continuum.[39,40] This region is dominated by scattering events of the outgoing electron on neighboring atoms and consequently the EXAFS region is best understood in terms of the wave behavior of the photo-electron created in the absorption process. The waves of the outgoing and scattered photo-electrons will interfere with each other. The interference pattern created depends on the path length of both waves and consequently the pattern contains information about the local structure around the absorbing atom. The EXAFS can be described by the EXAFS equation

$$\chi(k) = \sum_j \frac{N_j e^{-2k^2\sigma_j^2} e^{-\frac{2R_j}{\lambda(k)}} f_j(k)}{kR_j^2} \sin\left[2kR_j + \delta_j(k)\right] \tag{5}$$

where k is the photo-electron wave number, N is the number of neighboring atoms, $f(k)$ and $\delta(k)$ are the scattering factors of atoms neighboring the excited atom, R is the distance from the absorber atom, $\lambda(K)$ is the mean-free-path of the photo-electron and σ^2 gives the disorder in the neighbor distance. When the scattering factors $f(k)$ and $\delta(k)$ are known, the EXAFS equation enables us to find the number of neighboring atoms, distances to neighboring atoms and the disorder in this distance. Furthermore, the scattering factors $f(k)$ and $\delta(k)$ are dependent on the atomic number Z and as a consequence EXAFS is sensitive to the atomic species of neighboring atoms. Due to the (k) and R^2 terms, the EXAFS provides a quantitative local probe.

2.2.1 EXAFS analysis. In order to extract the EXAFS from experimental data, several steps must be taken.[40] To eliminate absorption from other edges and the instrumental background signal, the pre-edge background should be removed from the EXAFS spectrum. Subsequently, the ionization potential is determined to calculate k (Å^{-1}) *via*

$$k = \sqrt{\left(\frac{8\pi^2 m}{h^2}\right)\left(h\nu + E_0 + E_{\text{edge}}\right)} \tag{6}$$

The ionization potential can be determined by several methods, discussed previously in the XANES theory. Next, the total absorption should represent the absorption of 1 X-ray and normalized from 0 to 1. Thereafter the atomic post-edge background should be removed. The post-edge background is often approximated by a cubic spline function as described by Cook *et al.* (1981)[41] with care taken to ensure no loss in the oscillation information. A radial distribution function $\chi(R)$, where R is again defined as the distance from the absorber atom, is obtained by Fourier transformation (FT) of $\chi(k)$. Due to the scattering phase-shift, the real distance is 0.2–0.5 Å; longer than the distance found by FT. By using different k weightings, specific scatterers can be emphasized, *e.g.* multiplication by k^2 will emphasize oscillations at high k. The Fourier transform is a complex function, containing both an imaginary and a real part. The imaginary part gives mainly information about the absorber–scatterer distance, whereas the real part is mainly given by the number of neighboring atoms and disorders. However, the analysis of metal–metal bonds from EXAFS is not always unambiguous and often there are alternative solutions that are (mathematically) as likely as the calculated results. Fig. 6 gives an example of the results obtained after EXAFS data reduction.

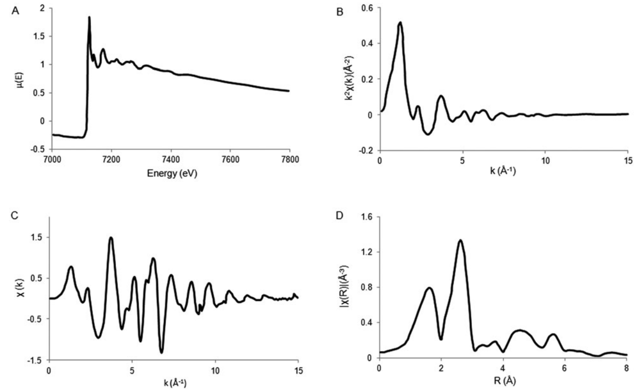

Fig. 6 Schematic representation of EXAFS data reduction. (A) XAS spectrum $\mu(E)$. (B) Isolated EXAFS $\chi(k)$. (C) k-weighted EXAFS $k^2\chi(k)$. (D) Fourier transformed EXAFS spectrum, $\chi(R)$. Adapted with permission from ref. 40.

2.3 Resonant inelastic X-ray scattering based XAS techniques

In this section we discuss a number of relatively novel X-ray spectroscopy techniques that are based on resonant inelastic X-ray scattering (RIXS). This includes high-resolution fluorescence-detected (HERFD) XAS and valence selective XAS. RIXS, also known as resonant X-ray emission spectroscopy (RXES), is a second order technique in which XAS and XES are combined.[42,43] The absorption of an X-ray photon with incident energy results in the excitation of a core electron. The core hole will be filled by the decay of an electron from a shallow core state or a valence state resulting in the emission of a photon. If the incident X-ray energy is chosen at an XAS edge, this X-ray emission is indicated as RIXS or alternatively as resonant X-ray emission or resonant X-ray Raman scattering. RIXS is a second order X-ray process where the excitation and de-excitation processes are coherently described by the Kramers–Heisenberg equation:

$$F(\Omega,\omega) = \sum_j \left| \sum_i \frac{\langle j|T_2|i\rangle\langle i|T_1|g\rangle}{E_g + \eta\Omega - E_i + i\Gamma_i} \right|^2 \delta\left(E_g + \eta\Omega - E_j - \eta\omega\right) \tag{7}$$

The scattering factor F is given as a function of the used X-ray energy (Ω) and the emitted X-ray energy (ω). The transition from the ground state (g) to the intermediate state (i) and subsequently to the final state (f) is described by the operators T_1 and T_2. The core-hole lifetime in the intermediate state Γ_i gives rise to spectral broadening. Experimentally RIXS can be divided into soft X-ray RIXS using grating optics and hard X-ray RIXS using bent crystal optics. In this review we limit our discussion to hard X-ray RIXS at the metal K edges. For recent developments in soft X-ray RIXS we refer to a recent (review) paper.[42] The RIXS resolution has been improved to 30 meV at 1 keV primary beam, where we note that due to the low efficiency of the high-resolution RIXS process *in situ* experiments are tedious.

When a 1s core hole is created by X-ray absorption radiative decay from 2p to 1s has the highest probability. These transitions are denoted as 1s2p RIXS or alternatively as Kα RXES. This notation describes the location of the core hole in the intermediate (1s) and final state (2p). Lower probability decay transitions also occur, for example Kβ XES, the decay from the 3p to 1s level. During a RIXS experiment the incident energy as well as the emitted energy is varied. The intensities for both energies are plotted in a two-dimensional plane, the RIXS plane. In this plane the x axis represents the incident energy and the y axis represents either the energy transfer or the X-ray emission energy. If the energy transfer is used in the 1s2p RIXS, the y-axis relates to an L edge, whereas the x-axis indicates the K edge. The lifetime broadenings of the L edge and K edge invoke vertical respectively horizontal Lorentzian broadenings. The experimental resolution is approximated with a Gaussian shape and applies horizontal for the incoming X-rays and diagonal for the X-ray analyzer. Fig. 7 shows the cobalt 1s2p RIXS plane.[43] The pre-edge excitonic states are visible at 7709 eV. The diagonal bands starting at 7714 eV are the 1s2p fluorescence bands.

A 45 degree diagonal cross section through the 1s2p RIXS plane implies a constant X-ray emission energy. This cross-section is indicated as the HERFD-XANES spectrum, where deviations can occur at the pre-edge region due to the excitonic effects. In HERFD spectra the spectral resolution is mainly determined by the lifetime broadening of the final 2p states and the experimental resolution. Because the 2p lifetime broadening is only 0.4 eV (full-width at half-maximum) 1s XANES spectra can be measured with 0.4 eV broadening instead of the natural lifetime broadening of ∼1.5 eV. Fig. 7 shows the comparison between XANES and HERFD-XANES of $LiCoO_2$ measured simultaneously.[44]

2.4 Soft X-ray experiments

The characterization of water oxidation catalysts using K-edge XAS has been extensive. K-edge XAS has been a valuable tool to approximate the electronic and structural properties that lend itself to OER catalysis. However, many of these studies were unable to distinguish distinct differences in XAS spectra among inactive and active catalyst systems.[45–48] In order to further the fundamental understanding of the structure–activity relationship, other X-ray techniques may need to be additionally employed, such as L-edge XAS and oxygen K-edge XAS.

2.4.1 Metal L-edge XANES. The functionality of WOCs is to a large extent influenced by the occupied and unoccupied 3d valence states of the catalyst material. Therefore, investigation of the 3d states can contribute to elucidating the structure–activity relationship of water splitting catalysts. The pre-edge structure of K-edge XAS gives information about transitions from the 1s to 3d states. Metal L-edge XAS offers a powerful tool to probe the unoccupied 3d states as it excites $2p^63d^n \rightarrow 2p^53d^{n+1}$ transitions. L-Edges for 3d transition metals are found in the soft X-ray regime (400–1000 eV) that can be measured with a resolution of ∼0.2 eV compared to ∼1.5 eV for hard X-rays. The 2p core state and the 3d valence state have a large overlap and therefore their interaction cannot be neglected. As a consequence the single electron excitation approximation is no longer valid. The initial state can then be written as a $3d^n$ wavefunction, whereas the final state can be written as a $2p^53d^{n+1}$ wavefunction. The electric dipole operator can then be written as

$$|\langle\phi_f|r|\phi_i\rangle|^2 = |\langle 2p^53d^{n+1}|r|3d^n\rangle|^2 \quad (8)$$

Due to the overlap between the core and valence states, the spin-moment of the core hole interacts with the valence electrons, resulting in an exchange splitting. If the core hole also carries an orbital momentum, as is the case for 3d metals, the spin–orbit coupling separates the 2p levels into $2p_{3/2}$ and $2p_{1/2}$, referred to as the L_3 and L_2 edge, respectively. The effects caused by the overlap of the core and final states are called multiplet effects. In the presence of spin–orbit coupling, the orbital angular momentum L and the spin angular momentum S are no longer appropriate to describe the system. The only valid quantum number in this case is the total angular momentum quantum number J. For the transition metal L-edges, p core

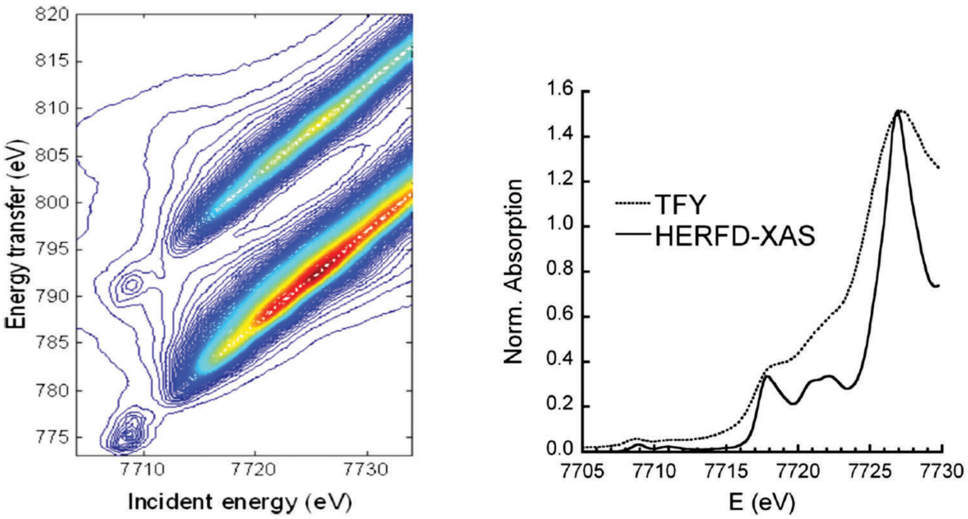

Fig. 7 (left) The experimental 1s2p RIXS plane of CoO. The red color indicates the highest intensity. Reprinted with permission from ref. 43. Copyright 2013 American Chemical Society. (right) The comparison between XANES (dotted) and HERFD-XANES (solid) spectra of $LiCoO_2$. Reprinted with permission from ref. 44. Copyright 2010 by the American Physical Society.

states are dominated by a large core hole spin–orbit coupling. In the presence of spin–orbit coupling, the selection rules for the orbital angular momentum and spin angular momentum are no longer valid and the new selection rule states that the total quantum number J can change by minus one, zero and one ($\Delta J = -1, 0, 1$). In addition, the value of the final state cannot be equal to zero if the J value of the initial state is zero ($J_i = J_f \neq 0$). The intensity ratio between the L_3 and L_2 edge is referred to as the branching ratio.[49] This parameter is sensitive to the spin state and spin–orbit splitting.

The 3d metal L-edges are sensitive to changes in the formal oxidation state. Due to the exchange splitting described above, the spectral shape of the metal L-edge is a complex multi-peaked structure. Therefore, rather than the edge position, the center of gravity of the complete L-edge is linearly related with the valence.

Fig. 8 shows an *in situ* L-edge experiment on a Co_3O_4 sample.[50] The temperature is increased while the sample is in a chamber with 1 mbar pure H_2 and during the heating procedure Co_3O_4 is changed to mainly CoO at 250 °C and to dominantly cobalt metal at 425 °C. This type of *in situ* L-edge data is best quantified with the use of references and also use of data analysis programs such as BluePrintXAS.[51]

2.4.2 Oxygen K-edge XANES. The importance of the hybridization of the oxygen 2p states with the metal 3d bands in electrocatalysis is described by J. Suntivich *et al.*[52–54] It was suggested that an increased character of the O 2p state near the Fermi level (E_f) allows the metal 3d states to mix with oxygen. Due to the increase in electronegativity by the oxygen electron injection and extraction is promoted, leading to higher OER activity. When a ligand, such as oxygen, is bound to an open shell metal ion, the ligand K-edge XAS spectrum provides information about the metal–ligand bonding interaction and electronic structure of the site, suggesting that oxygen K-edge XAS can be a valuable technique for obtaining a better structure–activity relationship for WOCs. Similarly to metal K-edge XAS, the core hole interactions in the final state of the ligand K-edge absorption are relatively weak. Therefore the XAS spectral shape of the ligand K-edge can be described with single electron approximation and the XAS spectral shape corresponds well with the p-projected density of states.[29] Analysis of the ligand K-edge indicates that the pre-edge intensity can be related to the hybridization of the ligand 2p with the metal 3d states.[55] Quantification of this structure gives the total hybridization of the ligand 2p with the metal 3d band, which is related to the metal–ligand covalence. The second region reflects ligand 2p character hybridized with the 4sp band. Ligand K-edge XAS probes a specific metal–ligand bonding interaction, rather than probing the net effect of the entire ligand environment as is done in metal L-edge XAS.[56]

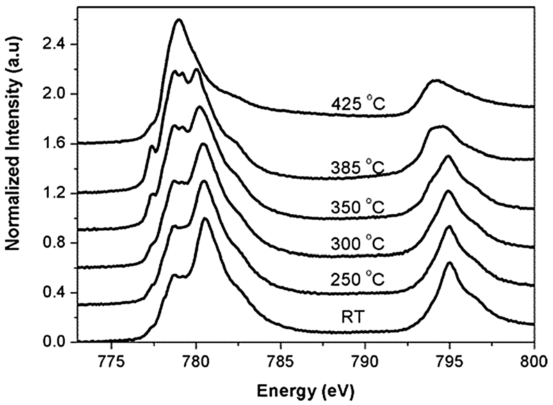

Fig. 8 Co $L_{2,3}$ edges for bulk Co_3O_4 during reduction from RT to 425 °C. All spectra have been normalized from zero to one. Reprinted with permission from ref. 50. Copyright 2004 American Chemical Society.

3 *Ex situ* metal K,L-edge XAS experiments

Ex situ XAS experiments are used to study WOCs as-prepared, upon synthesis or after being active in the water oxidation reaction. The synthesis itself in many cases involves applying a voltage or light illumination. *Ex situ* implies that a ground state atomic and electronic structure of the as-prepared catalyst at a given solution pH is investigated. This section reviews the XAS and EXAFS structural studies of as-prepared Co-, Mn- and Ni-based WOCs, gives an overview of the results, and reports the results in Table 2.

3.1 Cobalt-based WOCs

3.1.1 CoCat. A promising Co-based WOC, referred to as CoCat, was reported by Kanan and Nocera in 2008.[57] They reported a thin film catalyst that could be easily prepared upon oxidative polarization of indium tin oxide ($InSnO_3$) in a phosphate (P_i) buffer from reactant Co^{2+} ions in aqueous solution. The catalyst showed remarkable catalytic activity at low over-potential, neutral pH, room temperature and 1 atm. Furthermore, the catalyst exhibited a self-healing mechanism, similar to that observed in the biological Mn-complex of photosystem II. The electronic structure of this CoCat thin film was studied using XAS.[58,59]

The Co K-edge XANES structure of the KP_i-CoCat, compared to Co^{2+} and Co^{3+} standards, indicated a Co oxidation state of ∼3+ (Fig. 9). The spectral shape of the Co XANES region revealed information on the coordination geometry and ligand type and suggested a near-octahedral coordination of Co by six oxygen ligands (CoO_6).

EXAFS simulations verified the coordination of Co by six oxygen ligands (Fig. 10). A Co–O distance of 1.89 Å was found. A Co–Co distance of 2.81 Å suggested Co atoms interconnected by di-μ-oxo ($(\mu_3\text{-}O)_2$) or (μ_3-O)(μ_2-OH) bridges, as found in Co-oxo cubanes (Fig. 11). Furthermore, a Co–Co distance of 5.62 Å as second nearest neighbor indicates two cubanes sharing a Co corner. XAS also probed the orientation of the Co complex. By performing measurements at different angles between the X-ray beam and the sample surface, the catalyst showed a fully isotropic distribution of Co–O and Co–Co vectors, as was expected for cubane units.

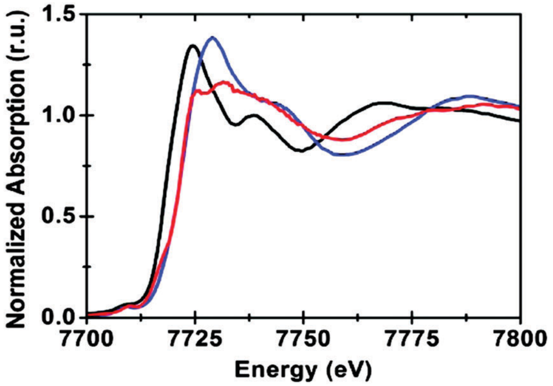

Fig. 9 The Co K-edge XANES structure of the CoCat (blue) and two references: $[Co^{II}(OH_2)_6](NO_3)_2$ (black) and $[Co^{III}(NH_3)_6]Cl_3$ (red). Reprinted with permission from ref. 58. Copyright 2009 American Chemical Society.

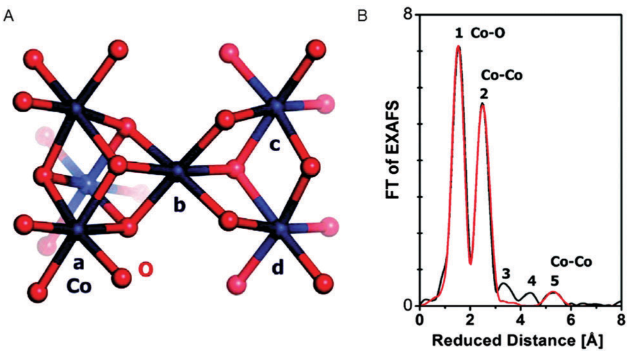

Fig. 10 (A) Interconnected incomplete and complete $Co_{3/4}(\mu\text{-}O)_4$ cubane units of CoCat (cobalt in blue, oxygen in red). (B) FT of an EXAFS structure of CoCat catalyst. The black line represents the experimental spectrum, whereas the red line indicates an EXAFS simulation. Reprinted with permission from ref. 58. Copyright 2009 American Chemical Society.

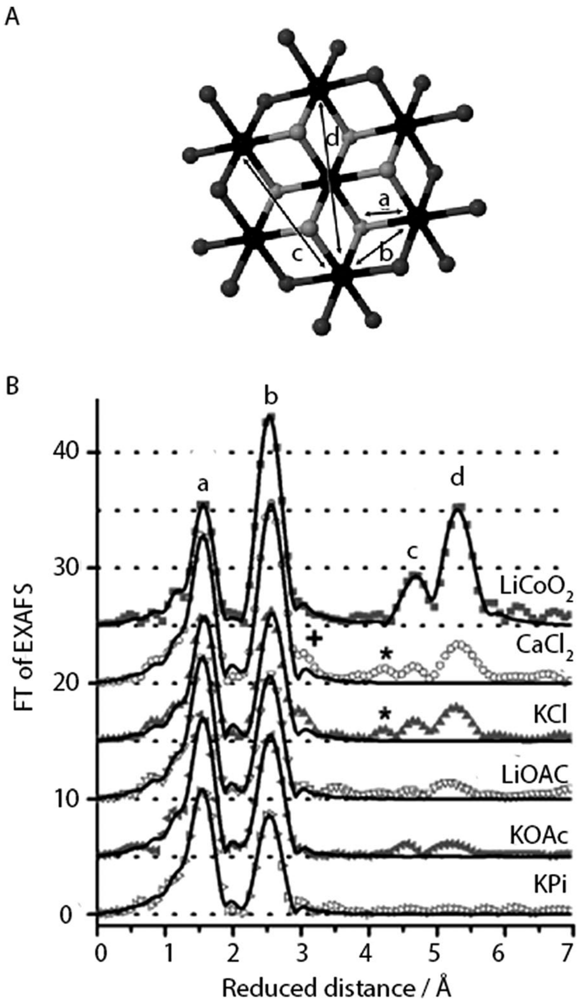

Fig. 11 (A) CoCat fragment showing the prevalence of Co-oxido motifs (cobalt in black, μ_3-O in grey, oxygen atoms that could be protonated or stemming from the anionic ligands in dark grey). (B) FT of an EXAFS structure of CoCat catalysts prepared in different electrolytes. Peaks marked by a, b, c and d refer to the Co-oxido structure in panel A. Reprinted with permission from ref. 59. Copyright 2012 John Wiley and Sons.

To test the stability of the CoCat, additional XAS measurements were performed on a dried CoCat ground to a powder, dried CoCat on $InSnO_3$ electrodes and a quasi *in situ* condition, where the CoCat-covered cathode was rapidly removed from the solution and frozen in liquid nitrogen. The XANES and EXAFS region of all this sample set looked similar, suggesting the CoCat is robust against air exposure, dehydration and mechanical treatment.

The composition of the CoCat films was shown to be dependent on electrolyte composition, pH and Co concentration during electrodeposition.[60] The influence of different electrolyte compositions on the structure and function of the CoCat films was further studied.[59] In addition to the potassium phosphate buffer, different CoCats were prepared at pH 7 from weakly buffering acetate electrolytes, KOAc and LiOAC, and non-buffering chloride electrolytes, KCl and $CaCl_2$. Despite the compositional differences noted by Surendranath (2009), the functionality of the various CoCat films was only weakly dependent on the redox-inert cation. In addition, XANES showed that the Co oxidation state was still ~3+ for all CoCats as shown in Table 1 and EXAFS revealed that the Co ligand environment was also similar to the structure previously reported for KP_i-CoCat, except for KCl-CoCat.

The pre-edge intensity of the CoCat samples was found to be higher when compared to the Co^{2+} reference. The increase of pre-edge intensity with oxidation state could be explained by the shortening of the metal–oxygen distances upon oxidation, resulting in increased mixing between the p and d orbitals.[61] Furthermore, variation in the pre-edge intensity between the different CoCats may indicate varying amounts of short di-μ-oxido bonds, as highly symmetric arrangements of ligands lead to a decrease in pre-edge intensity.[62]

FT analysis of the EXAFS structure of the CoCat samples reflects a reduction in order when compared to the crystalline $LiCoO_2$ reference as indicated by the low amplitudes of the FT peaks b, c and d (Fig. 11). The highest degree of order was found for the least active KCl-CoCat, whereas the lowest degree of order was observed for the most active KP_i-CoCat. Consequently, it was hypothesized that the active species of the CoCat films were peripheral Co-oxido clusters, with the terminal O atoms

Table 1 Edge position and oxidation state (O.S.) found for various CoCat films prepared in different electrolytes. Reproduced with permission from ref. 59. Copyright 2012 John Wiley and Sons

Sample	Edge position (eV)	O.S.
KP_i-CoCat	7721.0	3.1
LiOAc-CoCat	7721.0	3.1
KOAc-CoCat	7720.8	3.0
KCl-CoCat	7719.8	2.6
$CaCl_2$-CoCat	7720.7	3.0
$Co^{2+}(OH)_6$	7718.6	2.0
$LiCo^{3+}O_2$	7720.9	3.0

and possibly the O-atoms in μ_2-O bridges of the metal oxide playing an important role in water oxidation catalysis.

3.1.2 Homogeneous catalysts: Co-POMs. Co polyoxymetalates (POMs) are efficient WOCs and are often viewed as a more structurally defined version than CoCat.[57,63–65] However, significant differences in water oxidation activity have been reported for different Co POM structures. While some do not exhibit any water oxidation activity,[66] Co POMs that contain a cobalt tetramer core generally exhibit significant water oxidation activity dependent on adatoms and the ligand environment. For example, Yin *et al.* reported a turnover frequency (TOF) of $\geq 5\ s^{-1}$ for a $Na_{10}[Co_4(H_2O)_2(\alpha\text{-}PW_9O_{34})_2]\cdot nH_2O$ Co-POM, and a TOF as high as 1000 s^{-1} was reported by Lv *et al.* for a $Na_{10}[Co_4(H_2O)_2(VW_9O_{34})_2]\cdot 35H_2O$ Co-POM;[64,67] the two structures only differ in the adatom (W *vs.* V). As a result, various studies have applied XAS to determine the electronic structure differences that may exist to explain differences in catalytic activity.[46,65] They primarily concern the Co POMs shown in Fig. 12, where (1) and (2) have an identical Co tetramer core with different POM ligands, (3) is similar to (1) but with a different phase of the POM ligand, and (4) contains two sets of cores composed of three cobalts each. Except for (2), the Co POMs shown exhibit significant water oxidation activity. In the following, the Co K-edge XAS results for the four Co POMs are reviewed. Co L-edge XAS of various Co POMs is discussed at the end.

Ohlin (2011) investigated $K_{10}[Co_4(H_2O)_2(\alpha\text{-}PW_9O_{34})_2]\cdot 26H_2O$ (1) and the Wells–Dawson sandwich, $Na_{16}[Co_4(H_2O)_2(\alpha\text{-}P_2W_{15}O_{56})_2]\cdot 52H_2O$ (2) (Fig. 12). Despite having an identical cobalt tetramer core, (1) was found to be active in water oxidation, whereas (2) did not show any water oxidation activity.[46] This suggested that ligands play an important role in tuning the stability and catalytic activity of the Co POM complexes. Since water oxidation is most likely situated on two terminal Co atoms, which coordinate with water, it was suggested that ligand effects on the terminal cobalt atoms tune activity.[46] Co K-edge XAS spectra were acquired for solids and solutions of (1) and (2). The XANES structures for both catalysts in solid state and in solution are similar. The edge position and spectral shape indicate the presence of a Co^{2+} species in both catalysts. The EXAFS structure for both Co POMs shows two major peaks, where the first peak is related to Co–O bonds, giving a Co–O distance of ~1.9 Å, and the second peak is related to a disordered group of single-scatter vectors assigned to Co–Co and Co–W bonds, suggesting a M–M distance of ~3.2 Å. The FT EXAFS showed no significant differences between the solid state and the solution state sample except for a slight intensity increase in the second peak for the solvated samples, indicating a slightly more ordered state, as shown in Fig. 13. No significant differences between the two structures were found within the XAS spectra, suggesting that the difference in activity cannot be solely attributed to ligand effects on the terminal cobalt atoms.

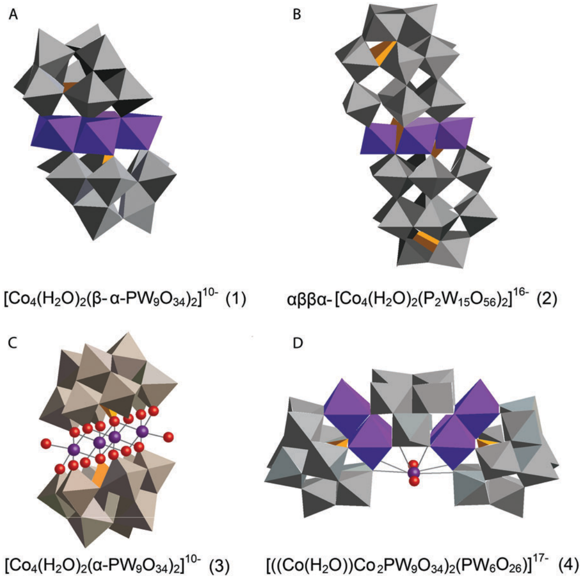

$[Co_4(H_2O)_2(\beta\text{-}\alpha\text{-}PW_9O_{34})_2]^{10-}$ (1) $\alpha\beta\beta\alpha\text{-}[Co_4(H_2O)_2(P_2W_{15}O_{56})_2]^{16-}$ (2)

$[Co_4(H_2O)_2(\alpha\text{-}PW_9O_{34})_2]^{10-}$ (3) $[((Co(H_2O))Co_2PW_9O_{34})_2(PW_6O_{26})]^{17-}$ (4)

Fig. 12 Co POMs studied by Ohlin (2011) and Schiwon (2014): (A) $K_{10}[Co_4(H_2O)_2(\alpha\text{-}PW_9O_{34})_2]\cdot 26H_2O$ (1); (B) the Wells–Dawson sandwich, $Na_{16}[Co_4(H_2O)_2(\alpha\text{-}P_2W_{15}O_{56})_2]\cdot 52H_2O$ (2); (C) $Na_{10}[Co_4(H_2O)_2(PW_9O_{34})_2]$ (3) and (D) $Na_{17}[((Co(H_2O))Co_2PW_9O_{34})_2(PW_6O_{26})]$ (4)[46,65] (Co^{II}-octahedra in violet, tungstate ligands in grey, phosphorus heteroatoms in orange, and oxygen atoms depicted as red spheres).

The stability of the Co POM catalyst (1) in solution was investigated by taking XAS spectra at various pH values. The Co K-edge XANES structure did not change as a function of pH and remained consistent with a Co^{2+} species. Additionally, small changes in pH from 7.5 to 6.5 did not show any major changes in the FT EXAFS structure. However, as the pH was reduced from 7.5 to 2.5, the FT showed an increase in the first peak, accompanied by a reduction of the second peak, suggesting dissociation of the cluster to free Co^{2+} in solution. These results indicate that the POM clusters are stable in near-neutral and slightly acidic environments, but will dissociate in strongly acidic solutions.

Schiwon *et al.* (2014) investigated the stability of the active Co POM, $Na_{10}[Co_4(H_2O)_2(PW_9O_{34})_2]$ (3), in both solution and solid state by using Co K-edge XAS.[65] The structure of Co POM (3) is depicted in Fig. 12. XAS spectra were acquired for both solid state and solutions of (3). The XANES structures obtained for different concentrations of (3) in aqueous solutions do not show significant differences from each other and are similar when compared to the solid sample of (3). XANES edge positions give a Co oxidation state of 2+. This oxidation state was conserved upon dissolution of the microcrystalline powder and after Ru^{III}-driven water oxidation catalysis. Analysis by comparing (3) to another Co POM with a well known structure,

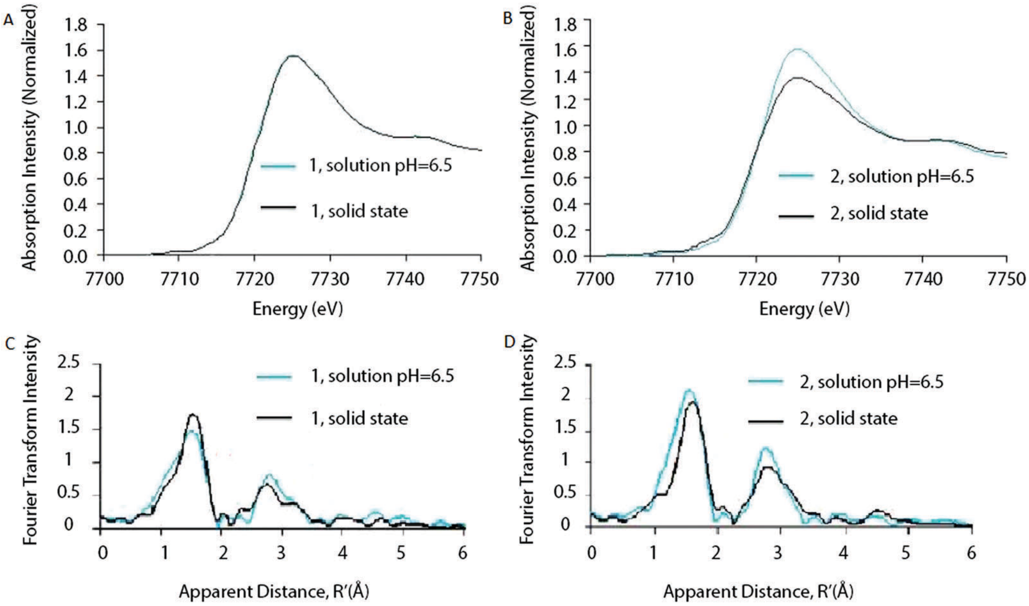

Fig. 13 XANES of (A) Co POM (1) and (B) Co POM (2) and FT of the EXAFS structures of (C) Co POM (1) and (D) Co POM (2). XAS structures are given for both Co POMs in solution as well as in solid state. Reprinted with permission from ref. 46. Copyright 2011 John Wiley and Sons.

$Na_{17}[((Co(H_2O))Co_2PW_9O_{34})_2(PW_6O_{26})]$ (4) (Fig. 12), confirmed the sensitivity of XAS to small amounts of dissociated Co^{2+} ions. While (3) has four Co within the core structure, (4) has three Co. The coordination number found by EXAFS simulations predicts a difference of one Co atom between these two structures, concluding that the loss of a single Co ion through dissociation would be detectable by EXAFS analysis. Furthermore, EXAFS analysis indicates a M–M distance of 3.19 Å for (3) in both solid and liquid phases, whereas for (4) a M–M distance of 3.8 Å was found. For both (3) and (4) a Co–O distance of $\sim$2.05 Å was reported.

Both XANES and EXAFS confirmed that neither dissolving nor oxidant exposure and water oxidation catalysis modifies the structure of (3), revealing a stable (3) under experimental conditions. The XANES structures of the Co POM (3) before and after catalysis were found to be significantly different from $[Co(H_2O)_6]^{2+}$ and the typical edge-sharing octahedra found in CoCat, suggesting the absence of dissociation of (3) into free Co^{2+} ions which could form a CoCat-like structure upon electro-oxidation as previously suggested by Stracke *et al.*[68]

Hibberd and co-workers (2015) used Co L-edge XAS to study the electronic structure of various Co POMs and Co_3O_4 thin films.[66] L-Edge XAS spectra for the Co POMs determined the oxidation state, ligand coordination geometry, and the effects of electron–electron interactions on Co–O hybridization. While providing a thorough understanding of the ground state electronic structure, the Co L-edge structure was insensitive to the heteroatom identity and number and position of Co ions that differentiate the activity of the different Co POMs.

3.2 Nickel-based WOCs

Dinça and co-workers reported on electrodeposited Ni oxide WOCs (NiCats), similar to the electrodeposited CoCat reported by Nocera *et al.*, which show reasonable water oxidation activity under ambient conditions.[57,69] Risch and co-workers (2011) used XAS to study the electronic and atomic structure of two active NiCats, synthesized either from a phosphate buffer at pH 7 or from an aqueous borate (B_i) buffer at pH 9.2.[70] Ni K-edge XANES studies indicated that the oxidation state of the KP_i-NiCat was close to Ni^{3+}, whereas that of the B_i-NiCat was between Ni^{3+} and Ni^{4+}. Ni–O bond lengths obtained from EXAFS analysis allowed a more accurate determination of the B_i-NiCat oxidation state. Using a relation between the Ni–O bond length and Ni oxidation state obtained from the literature, the oxidation state was found to be 3.8+ for B_i-NiCat. EXAFS analysis of the B_i-NiCat suggested a layered γ-NiOOH-like structure, with borate and water molecules between the oxide layers. Comparison of the EXAFS spectra of B_i-NiCat and CoCat indicated a similar layered oxide structure for both catalysts, as shown in Fig. 14.[58] Comparison of the Ni–Ni bond length of the B_i-NiCat to CoCat indicated a common M–M distance of 2.81 Å, indicating the presence of di-μ-O(OH) bridging between metal ions for both NiCat and CoCat. The higher intensities of the peaks at reduced distances of 4.9 Å and 5.6 Å indicated more long-range order for the NiCat than that observed for the CoCat. Overall, the atomic structure of the NiCat seems to be very similar to that of CoCat and several of the common features are also observed in the biological $Mn_4Ca(\mu\text{-}O)_n$ complex of photosystem II.[71]

A similar Ni-based catalyst was studied with XAS by Singh *et al.* (2013).[45] They investigated a NiO_x WOC electrodeposited from $[Ni(en)_3]Cl_2$, with en = 1,2-diaminoethane, in a 0.10 M borate buffer solution at pH 9.2. Both Ni K-edge XANES and EXAFS showed spectral shapes consistent with γ-NiOOH films, confirming the results by Risch and co-workers.[70]

Sun and co-workers (2012) used L-edge XAS to determine the oxidation state of Ni in a NiO_x functionalized silicon and

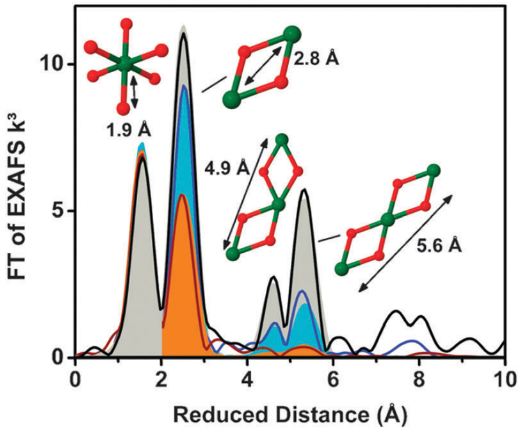

Fig. 14 FT of the EXAFS structures of (a) B_i-NiCat (blue) and (b) CoCat (red) and (c) crystals of layered Co oxide $LiCoO_2$ (black). Reproduced from ref. 70 with permission from the Royal Society of Chemistry.

found Ni^{2+} as the dominant species in both pre-annealed and annealed samples.[72]

3.3 Manganese-based WOCs

The Mn–oxide complex in nature's photosystem II is considered the most active water oxidation catalyst at low over-potentials.[73] The activity has in part been ascribed to a leveling of the potential by the distribution of Mn 3+ and 4+ oxidation states within the catalyst. Over the past few years, several studies have been conducted on the use of heterogeneous Mn oxides as catalysts for OER.[74,75] The water oxidation activity of most Mn-based systems is, however, drastically suppressed at neutral pH. Recently, *in situ* optical absorption studies suggested that surface associated Mn^{3+} ions act as precursors for OER.[76] At pH values lower than 9, Mn^{3+} decomposed to Mn^{2+} and Mn^{4+}. The lower water oxidation activity under neutral conditions was attributed to a lack of active Mn^{3+} ions.

XAS study on an electrodeposited Mn-based catalyst comparable to the CoCat presented by Nocera *et al.*[57] was reported by Zaharieva *et al.* (2012).[48] Voltage cycling was needed for this structure in order to get an active Mn catalyst which is in contrast with electrodeposited Co- and Ni-based catalysts, where electrodeposition at constant potential resulted in catalysis.[58,70] Mn K-edge XANES and FT EXAFS determined the structural differences between the inactive Mn oxide catalyst formed from electro-deposition at constant potential and the active catalyst prepared by a voltage-cycling protocol (Fig. 15). Mn K-edge XANES indicated an oxidation state of 3.8+ for the active Mn catalyst, whereas the inactive catalysts showed an oxidation state of 4.0+. The shape of the XANES spectrum of the inactive Mn oxide indicated a birnessite-type layered structure, whereas the active Mn catalyst suggested a less ordered ligand environment. The FT EXAFS spectra indicated coordination of the Mn by six oxygens at a distance of 1.89 Å and the presence of di-μ-oxo bridges for both materials, confirming the presence of $Mn^{IV}O_6$ in both the active and inactive phases. A difference in the peak intensities at higher reduced distances indicated a higher degree of order for the inactive Mn oxide.

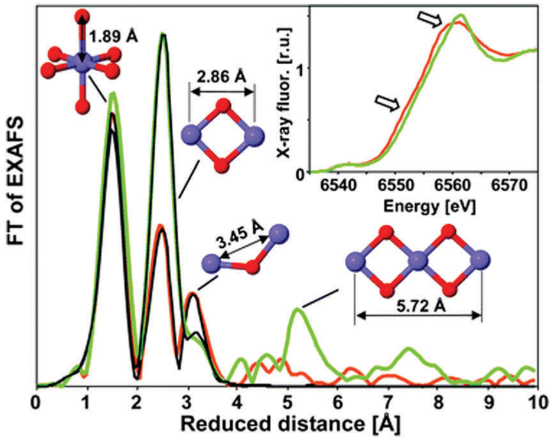

Fig. 15 XAS structures of the active MnCat (orange) and the inactive oxide (green). The FT EXAFS spectra are compared to EXAFS simulations shown in black. The inset shows the XANES region. Reproduced from ref. 48 with permission from the Royal Society of Chemistry.

The effect of calcination temperature on structure and catalytic activity was explored for a set of Mn-based WOCs using XAS on a highly active mesoporous MnO_x material[77] and a nanostructured Mn oxide cluster on silica.[78] The calcination temperature affected the Mn phase formed and the highest water oxidation activity was observed for the catalyst calcined at ~600 °C. Upon increasing the calcination temperature from 150 to 550 °C, Kuo *et al.* found that the Mn K-edge absorption edge showed a 0.4 eV energy shift towards higher energies, consistent with an increase in the oxidation state from 2.77 to 2.97.[77] However, Jiao *et al.* observed a slightly different trend at higher calcination temperatures ranging from 500 °C to 900 °C (Fig. 16). Analysis of the edge position on the nanostructured MnO_x cluster on silica indicated a decrease in the mean oxidation state from 4+ to 3+ to 2.85+ with increasing calcination temperature. Further analysis yielded fractional compositions of MnO_2, Mn_2O_3 and Mn_3O_4 at all calcination temperatures. Despite the opposite trend, both studies concluded that the catalyst with the highest activity

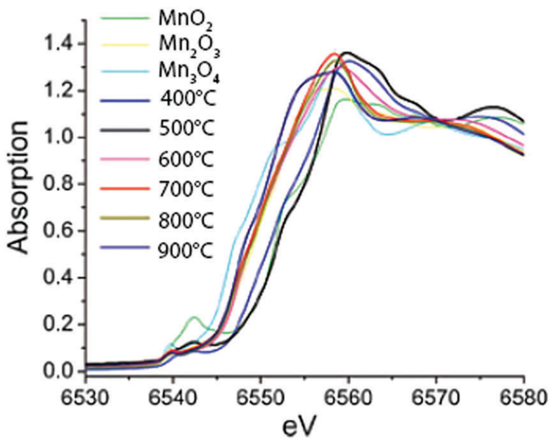

Fig. 16 XANES spectra of MnO_x materials calcined at different temperatures together with reference spectra of micron-sized particles of MnO_2, Mn_2O_3 and Mn_3O_4. Reproduced from ref. 78 with permission from the Royal Society of Chemistry.

consisted mainly of Mn_2O_3. Consequently, Mn^{3+} was suggested to be the most efficient species for water oxidation catalysis. Whereas the studies discussed above on Mn oxide catalysts claim the prevalence of a single structural polymorph, this finding was questioned by Robinson and co-workers (2013) based on the study on eight different Mn oxides containing Mn^{3+} and Mn^{4+}.[47]

Hocking *et al.* (2011) used XAS experiments to study the atomic structure of various Mn clusters in a Nafion polymer matrix[12] to determine the active species. The catalysts were synthesized by loading a tetra-nuclear Mn cluster $[Mn_4O_4L_6]^+$, with L = diarylphosphinate, a $[(bipy)_2Mn(O)_2Mn(bipy)_2]^{3+}$ complex and a $[Mn(OH_2)_6]^{2+}$ complex into Nafion. Significant water oxidation activity was only observed after electro-oxidation of the precursor complexes and was similar for the catalysts prepared from the different starting materials. This suggested that different Mn precursor complexes can lead to the same MnO_x catalyst film upon electro-oxidation.

Mn K-edge XANES and EXAFS spectra acquired for the three precursors in acetonitrile (reference), loaded into Nafion (precursor) and the active MnO_x catalyst formed after electro-oxidation of the precursor showed significant differences. The precursors showed an oxidation state of 2+, reduced from the reference oxidation state, while MnO_x catalyst had an average oxidation state of 3.75–3.85. EXAFS patterns of the three different Mn precursor materials loaded into Nafion had significantly different EXAFS structures, but upon electro-oxidation, gave similar EXAFS spectra. These patterns are consistent with the disordered $Mn^{3+/4+}$-oxide phase, which accommodates water and cations in the interlayer space (Fig. 17). Although the EXAFS structures of the three electro-oxidized products are similar, the product formed from the $[Mn(OH_2)_6]^{2+}$ precursor showed a more pronounced intensity at $k = 8$ Å^{-1}, indicating a more ordered lattice structure.[79]

Singh *et al.* (2013) found results consistent with Hocking *et al.* (2011).[12] The XAS spectra of two precursors, $[Mn^{IV}(Me_2TACN)(OCH_3)_3]^+$ (1) and $[(Me_3TACN)_2Mn_2^{III}(\mu\text{-}O)(\mu\text{-}CH_3COO)_2]^{2+}$ (2) (Fig. 18), that led to the most active WOCs were compared to a $[Mn(OH_2)_6]^{2+}$ precursor. XAS patterns of the parent compounds showed significantly different oxidation states and connectivity when compared to the electro-oxidized materials. Further, the Mn K-edge EXAFS patterns for the electro-oxidized product of (1), (2) and $[Mn(OH_2)_6]^{2+}$ showed no changes and matched well with the EXAFS pattern observed for natural and synthetic birnessite.

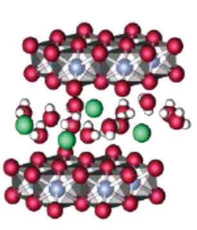

Fig. 17 Schematic representation of the crystal structure of birnessite, which consists of sheets of edge-sharing MnO_6 octahedra with intercalated cations and water in the interlayer space. $Mn^{4+/3+}$ is given in blue, oxygen in red, hydrogen in white and the cation in green. Reprinted with permission from ref. 80. Copyright 2013 American Chemical Society.

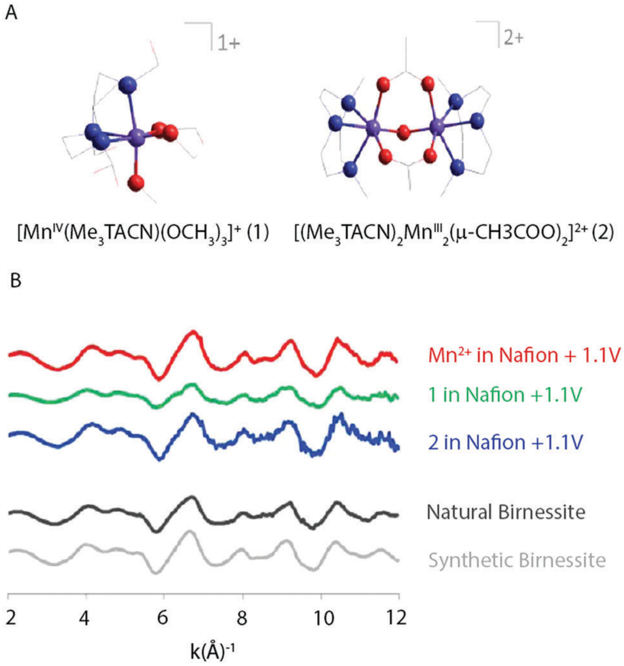

Fig. 18 (A) Structure of the two precursor complexes studied by Singh and co-workers. (B) k^3 weighted EXAFS spectra of the electro-oxidized products of Mn^{2+}, (1) and (2) in Nafion and natural and synthetic birnessite. Reproduced from ref. 45 with permission from the Royal Society of Chemistry.

The effect of light and applied potential on the precursor $[Mn_4O_4L_6]^+$ material for MnO_x was studied by Mn K-edge XAS experiments, as shown in Fig. 19.[12] State 1 is the precursor consisting of Mn^{2+} compounds. Upon applied potential, the edge position shifted towards higher energies, suggesting an oxidized $Mn^{3+/4+}$ product (state 2). When this oxidized $Mn^{3+/4+}$ was exposed to light in aqueous solution for 40 minutes, the edge position shifted towards lower energies, indicating photo-reduction back to Mn^{2+} (state 3). Subsequently when the

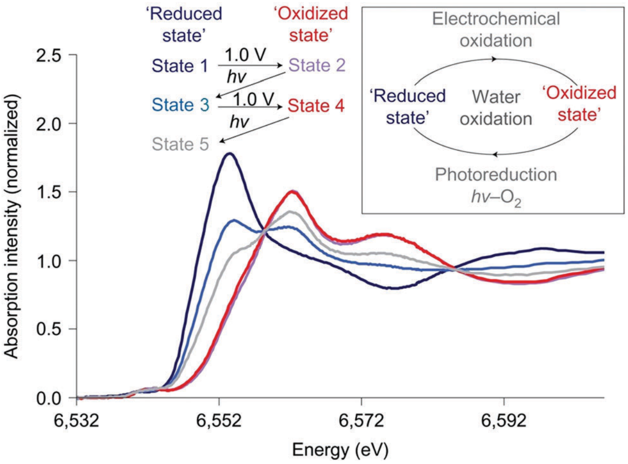

Fig. 19 Mn K-edge XANES spectra of the Nafion-coated $[Mn_4O_4L_6]^+$-loaded glassy carbon electrode. Spectra are measured at different states of photochemical cycling. Adapted by permission from Macmillan Publishers Ltd: Nature Chemistry (ref. 12), copyright 2011.

electrode was immersed in an electrolyte and a potential was applied again (state 4), re-oxidation to the $Mn^{3+/4+}$ species occurred. The electrode was then exposed to light for only 20 minutes (state 5) and afterwards XANES indicated a slow photo-reduction process. The study confirmed a self-healing mechanism to the active $Mn^{3+/4+}$ with applied potential from the reduced Mn^{2+} precursor state. The structure after light exposure, exposure to applied potential, and following water oxidation catalysis for 90 minutes was consistent with a $Mn^{3+/4+}$ oxidation state. The comparison of the XANES for the different states revealed two isosbestic points, suggesting a facile interconversion between Mn^{2+} and $Mn^{3+/4+}$ during water oxidation. Essentially, the Mn ions can assemble to form a high-surface area catalyst, similar to that observed for Nocera's CoCat.[57]

Mn L-edge XAS experiments by Kahn *et al.* (2014) indicate that Mn centers in MnO_x nanoparticles loaded and electro-oxidized in Nafion are highly oxidized.[81] Furthermore, a higher proportion of Mn^{3+} over $Mn^{2+/4+}$-like states was observed for the most active WOC. This is consistent with previous studies, where a greater proportion of Mn^{3+} species was associated with a local structural distortion and improved catalytic activity.[82]

3.4 Overview of metal K-edge XAS

K-edge XANES was used to study the oxidation state of various WOCs, whereas EXAFS provided information about the atomic structure of the metal atom, such as coordination number and bond-lengths of neighboring atoms. Table 2 gives an overview of the results found for the Co-, Ni-, and Mn-based WOCs.

Most of the WOCs had an average oxidation state of ~3+. While the CoCats are fairly close to a 3+ Co oxidation state, the KP_i-NiCat and MnCat had metal oxidation states that reached 3.8+. The MnO_x WOCs are close to a Mn 3+ oxidation state. Deviations from these oxidation states were correlated with lower activity. The KCl-CoCat, showing the lowest activity among the CoCats, gave a slightly lower average oxidation state of 2.6+. The inactive Mn oxide had a higher oxidation state of 4+.

The metal–oxygen coordination number (N_{M-O}) of ~6, the M–O bond length of ~1.9 Å and the metal–metal (M–M) bond length of ~2.8 Å were consistent among the solid state Co-, Ni- and Mn-based WOCs[12,48,59,70] and suggest that these WOCs have di-μ-O(OH) bridges with edge-sharing $M^{n+}O_6$ octahedra. Some exceptions to this structure are evident. A deviation from the M–O coordination (N_{M-O}) of ~6 was found for the active MnCat[48] and the least active CoCat KCl-CoCat,[59] both of which showed a N_{M-O} closer to 5. Furthermore, the metal–metal coordination number (N_{M-M}) varied most among the different WOCs, but showed no trend with water oxidation activity.

Various studies reported the use of EXAFS to probe the degree of order by analyzing the peak intensities at higher reduced distances. Most studies concluded that a lower degree of order resulted in higher water oxidation activity.[48,59,70] For Zaharieva *et al.*, this was the only clear difference in structure observed between the inactive and active Mn oxide materials.[48] Based on this trend, it has been suggested that less stable structures ensure availability of terminal coordination sites for binding molecular water species.[48,59]

Overall, the ground state atomic and electronic structures of the more active, as-prepared Mn, Co, and Ni oxide catalysts demonstrate significant similarities. They have a metal oxidation state of ~3+, are characterized by a M–O distance of ~1.9 Å, are comprised of di-μ-O(OH) bridges with edge-sharing $M^{3+}O_6$ octahedra, and exhibit structural disorder by EXAFS. The data also indicate that there are exceptions to these trends, though they cannot be correlated with activity. For the active CoCat, $Co_4(\mu\text{-}O_4)$ cubanes may also contribute and could not be excluded by EXAFS data.[58,59] The di-μ-oxo bridging, believed to be integral to the biological $Mn_4Ca(\mu\text{-}O)_n$ complex in photosystem II, was also present in the inactive Mn oxide.[48]

The homogeneous Co POM catalysts showed significant differences when compared to their heterogeneous counterparts. The 2+ oxidation state observed for the highly active molecular, homogeneous Co POMs was significantly lower than the oxidation state observed for the heterogeneous catalysts,

Table 2 Overview of the structural and electronic characteristics found by XAS and EXAFS for different WOCs. Catalysts marked with * are reported to be active in water oxidation catalysis

Ref.	Sample	State	Ox. state	N_{M-M}	M–M (Å)	N_{M-O}	M–O (Å)
Risch 2009[58]	KP_i-CoCat*	Upon electro-oxidation	3	—	2.81	6	1.89
Risch 2012[59]	KP_i-CoCat*	Upon electro-oxidation	3.1	3.3	2.81	6.0	1.89
	LiOAc-CoCat*	Upon electro-oxidation	3.1	3.9	2.82	6.1	1.89
	KOAc-CoCat*	Upon electro-oxidation	3.0	4.5	2.83	6.30	1.90
	KCl-CoCat*	Upon electro-oxidation	2.6	3.4	2.85	5	1.91
	$CaCl_2$-CoCat*	Upon electro-oxidation	3.0	5.3	2.84	6.5	1.90
Ohlin 2011[46]	Co-POM (1)*	Upon synthesis	2	—	~3.2	—	~1.9
	Co-POM (2)	Upon synthesis	2	—	~3.2	—	~1.9
Schiwon 2014[65]	Co-POM (3) (s)	Upon synthesis	2	2.5	3.19	6.0	2.05
	Co-POM (3) (l)	Upon synthesis	2	2.5	3.19	6.7	2.04
	Co-POM (4) (s)	Upon synthesis	2	1.5	3.8	6.5	2.05
Risch 2011[70]	B_i-NiCat*	Upon electro-oxidation	3.8	4.4	2.8	6.3	1.88
	KP_i-NiCat	Upon electro-oxidation	3	—	—	—	—
Zaharieva 2012[48]	MnCat*	Upon voltage cycling	3.8	2.6	2.86	5.3	1.89
	Mn oxide	Upon electro-oxidation	4	4.3	2.86	5.9	1.89
Kuo 2015[77]	MnO_x on silica*	Upon synthesis	3	—	—	—	—
Jiao 2010[78]	MnO_x on silica*	Upon synthesis	3	—	—	—	—
Hocking 2011[12]	Mn in Nafion*	Upon electro-oxidation	3.8	—	~2.9	6	~1.9
Singh 2013[45]	Mn in Nafion*	Upon electro-oxidation	—	—	—	—	—

but consistent among the various Co POMs. Co POMs (1) and (2) had a M–O bond length of ∼1.9 Å, whereas Co POMs (3) and (4) yielded slightly longer M–O bond lengths of ∼2.05 Å. The Co POMs with a core of 4 Co atoms showed a M–M bond length of ∼3.2 Å, whereas Co-POM (4), which has two metal cores with only 3 Co atoms each, gave a slightly higher M–M bond length of 3.8 Å.

4 *In situ* metal K-edge XAS experiments

Although *ex situ* XAS experiments are valuable to study the chemical structure of water splitting catalysts before or after reaction, the chemical state of a catalyst will change during a reaction, creating meta-stable intermediates. *In situ* XAS experiments provide the ability to study the structure and electronic properties of catalysts while a reaction is proceeding and can thereby contribute towards a better understanding of the structure–activity relationships, as the actual active phase can be monitored. The high X-ray energy needed for 3d metal K-edge XAS makes this technique extremely suitable for *in situ* experiments, as vacuum is not required and experiments can be performed under ambient conditions. Furthermore, at the X-ray energies needed for metal L-edge XAS or oxygen K-edge XAS, absorption of the electrolyte requires advanced set-ups, making L-edge *in situ* experiments challenging.

When applying a potential equal to or higher than the water oxidation onset and/or light illumination, ideally the transition metal oxide radical thought to be the catalytic intermediate required for O–O bond formation is created. This radical is created by the transformation of holes into a molecular species at the transition metal oxide/electrolyte interface. While under steady state current evolution the catalytic cycle turns over many times, a number of electrochemical and spectro-electrochemical experiments suggest that a large population of such transition metal oxide radicals are created at the electrolyte interface under steady state conditions.[8–10] Therefore, changes in oxidation state observed by steady state, *in situ* XAS should be reflective of these transition metal oxide radicals. However, under the conditions of steady state current evolution, one should keep in mind that XAS in principle monitors an average oxidation state of a dynamic system. The catalyst will be oxidized by hole injection due to the applied potential or light illumination and reduced by electron injection due to water oxidation. Furthermore, XAS is a bulk sensitive technique, and therefore an average oxidation state change of bulk and surface charge is measured. A higher oxidation state of the metal generated by reaction conditions, therefore, only indicates that surface metals have been oxidized and cannot determine whether a full oxidation state change has taken place. Since metal K-edge XAS dominates *in situ* studies of water oxidation catalysts, the information primarily concerns the metal oxidation state.

This section first reviews the XAS and EXAFS structural studies of Co-, Mn- and Ni-based WOCs under reaction conditions, then gives an overview of the results, and reports the results in Table 3.

Table 3 Overview of the structural and electronic characteristics found by *in situ* XAS and EXAFS for different WOCs. Applied potentials are given *versus* NHE, unless stated otherwise. (O.S. = oxidation state)

Sample	*In situ* conditions	O.S. change	O.S. *ex situ*	Structure
Co-P_i CoCat Kanan 2010[83]	Electrochem. OCV → 1.25 V	<3+ → >3+	∼3+ upon elec. ox.[58,59]	H_xCoO_2
Co-P_i CoCat on Au Friebel 2013[84]	Electrochem. −0.8 V → 1.0 V	3+ → >3+	∼3+ upon elec. ox.[58,59]	H_xCoO_2
Co_3O_4 spinel Bergmann 2015[85]	Electrochem. 1.0 V → 1.62 V *vs.* RHE	2+/3+ → 3+/4+	2.67 upon synth.[85,86]	Co_3O_4 → CoOOH
Co_3O_4 spinel Wang 2016[86]	Electrochem. 0.5 V → 1.0 V	2.67+ → 3+/4+	2.67 upon synth.[85,86]	Co_3O_4 → CoOOH
CoO_x NPs on CNT Seo 2016[87]	Electrochem. OCV → 1.8 V *vs.* RHE	2.4+ → 2.8+ (particle size: 6.3 nm)	—	Co_3O_4 and/or CoO → Co_3O_4 + CoOOH
Ni-B_i-Cat (non-activated) Bediako 2012[88]	Electrochem. 0.4 V → 1.0 V	2+ → 3.16+	3.8+ upon elec. ox.[70]	β-NiOOH
Ni-B_i-Cat (activated) Bediako 2012[88]	Electrochem. 0.4 V → 1.0 V	2+ → 3.6+	3.8+ upon elec. ox.[70]	γ-NiOOH
Ni-B_i-Cat Yoshida 2014[91]	Electrochem. 0.2 V → 1.1 V	2.1+ → 3.8+	3.8+ upon elec. ox.[70]	$Ni(OH)_2$ → γ-NiOOH
MnO_x/Au–Si_3N_4 Gorlin 2013[80]	Electrochem. −0.8 V → 1.0 V	2.8+ → 3.6+	3+ upon synth.[77,78]	Birnessite-like phase + $Mn_3^{II,III,III}O_4$
MnO_x/Nb:$SrTiO_3$ (film) Yoshida 2013[92]	Electrochem. −1.3 V → + 1.7 V	3+ → >3+	—	—
	Photo-electrochem. 1.2 V → 1.2 V + UV	2.8+ → 3.6+	—	—
MnO_x/Nb:$SrTiO_3$ (NPs) Yoshida 2013[92]	Photo-electrochem. 1.2 V → 1.2 V + UV	3+ → 2+/3+/4+	—	—
MnO_x/$SrTiO_3$ Yoshida 2014[93]	Photo-electrochem. 0.5 V → 0.5 V + UV	3+ → >3+	—	—
	Photo-electrochem. 0.0 V → 0.0 V + UV	3+ → >3+ (slow)	—	—
	Photo-electrochem. −0.5 → −0.5 + UV	3+ → 3+	—	—

4.1 Cobalt-based WOCs

The atomic and electronic structure of Nocera's Co-P$_i$ CoCat during active catalysis was studied by Kanan *et al.* (2010).[57,83] Both a thin surface film of approximately monolayer thickness and a thicker bulk film with $>10\times$ more material were studied in an *in situ* XAS experiment. Experiments studied the oxidized intermediate during catalysis at 1.25 V (all voltages are reported with respect to the normal hydrogen electrode (NHE) unless stated otherwise) and the electronic structure of the catalyst state when this potential is removed and the system is left at open circuit potential (OCP). The XANES structures for both the bulk and surface Co-P$_i$ films at 1.25 V and OCP are given in Fig. 20A.

The edge position indicated a Co valence state higher than 3+ for both the bulk and surface Co-P$_i$ films during water oxidation catalysis at 1.25 V. The inset in Fig. 20A shows the OCP *vs.* time traces, indicating that the Co-P$_i$ is returning to equilibrium at OC during this time. When switching from 1.25 V to the OCP, the absorption edge shows a continuous shift towards lower energies. This indicates that the metal is reduced due to electron injection from water caused by residual water oxidation. The edge-shift to lower energy was more pronounced ($\sim$1.0 V) for the thin film compared to the thick film ($\sim$0.3 V), indicating that a larger fraction of Co ions in the surface Co-P$_i$ sample are reduced compared to the bulk Co-P$_i$ sample within the time frame of the measurement.

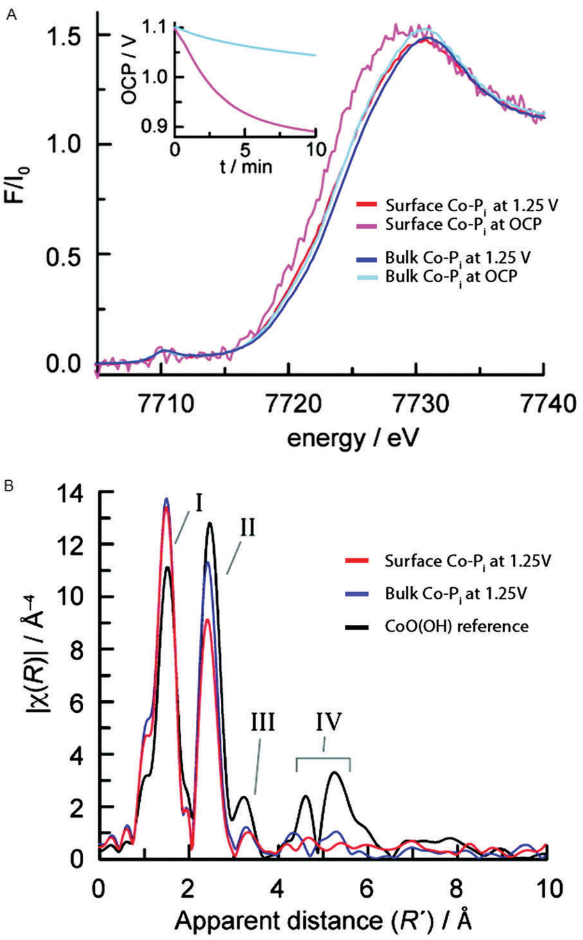

Fig. 20 (A) *In situ* XANES structures for the surface Co-P$_i$ at 1.25 V (red) and OCP (magenta) and the bulk Co-P$_i$ sample at 1.25 V (blue) and OCP (cyan). The inset shows the OCP traces for the bulk and surface films. (B) FT EXAFS structures for the bulk and surface Co-P$_i$ at 1.25 V are shown in blue and red, respectively. Black represents a CoO(OH) reference. Reprinted with permission from ref. 83. Copyright 2010 American Chemical Society.

FT EXAFS structures of the bulk and surface sample under a potential of 1.25 V and at OCP are shown in Fig. 20B. Two prominent peaks, I and II, were present and reflect the Co–O and Co–Co vectors respectively. The vectors indicated a Co–O distance of 1.89 Å and a Co–Co distance of 2.82 Å, indicating a similar edge-sharing CoO$_6$ octahedral CoCat structure as reported in the *ex situ* K-edge experiments by Risch and co-workers.[58,59] The higher intensity of the Co–Co vector (peak II) for the bulk sample indicated a larger average number of Co–Co vectors per Co ion, as can be expected when comparing a bulk sample to a surface sample. Peaks III and IV could be related to contributions from outer shells and their weak intensities indicated a low degree of order for the edge-sharing CoO$_6$ octahedra, again consistent with the *ex situ* experiments by Risch *et al.*[59]

In 2013 Friebel *et al.* studied the chemical state of a CoP$_i$ CoCat during water oxidation catalysis using a HERFD XAS mode.[84] HERFD XAS gives a more detailed spectrum due to a reduced lifetime broadening, making this mode suitable for studies of the weak pre-edge structure, caused by 1s → 3d transitions. Measurements were carried out under different potentials, ranging from −0.8 V to 1.0 V. The acquired HERFD XAS spectra are given in Fig. 21. Upon increasing the potential the main absorption edge shifts towards higher energy, indicating an increased amount of Co^{4+} species. At low potential the pre-edge structure shows a sharp peak at 7710.2 eV and a broader feature at 7712.5 eV. The peaks were assigned to both local and non-local transitions of high spin Co^{3+} in an octahedral environment. Local transitions involve the 1s3d quadrupole excitations and non-local transitions involve the 1s4p dipole transitions to the

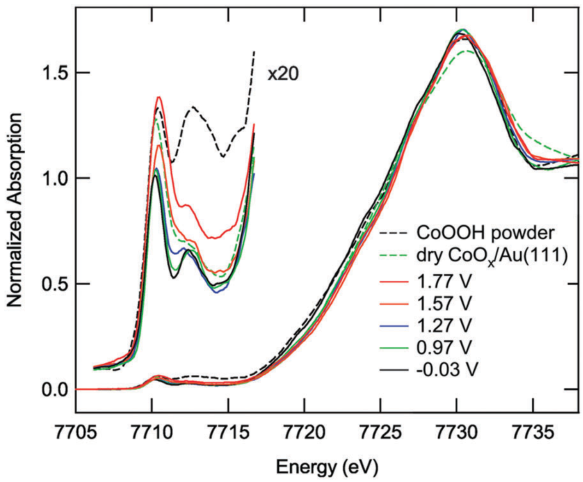

Fig. 21 *In situ* HERFD XAS structures of the Co-P$_i$-CoCat on Au at different potentials. Furthermore the spectra of a dry, as-prepared Co/Au sample and a CoOOH(s) reference sample are shown. Reproduced from ref. 84 with permission from the PCCP Owner Societies.

3d-band, where the energy difference is given by the core hole potential.[38] When switching to higher potentials, the sharp lower energy peak increases in intensity and broadens towards higher energy. Analysis of the changes in the pre-edge structure by least square fits suggested the presence of a third peak at 7710.9 eV, which is assumed to be a contribution from Co^{4+} ions in H_xCoO_2. Both edge and pre-edge analyses thus indicate that applying a potential results in oxidation of a fraction of the Co^{3+} species to Co^{4+}.

A slightly higher Co oxidation state was found for the CoCat in neutral phosphate buffer studied by Kanan[83] when compared to that of the CoP$_i$ in alkaline buffer studied by Friebel.[84] The difference in Co oxidation state was ascribed to different solubility of the Co^{2+} ions at various pH values. The high solubility of Co^{2+} at low pH results in the formation of small cobaltate clusters, whereas at higher pH, the solubility of Co^{2+} is reduced by 12 orders of magnitude. Therefore, at high pH, large aggregates of H_xCoO_2 form and limit the proton exchange *via* $CoOOH + (1 - x)OH^- \rightarrow H_xCoO_2 + (1 - x)H_2O + (1 - x)e^-$, with $x < 1$. This reaction hampers the proton exchange between CoOOH and H_2O and thereby impedes the formation of new oxidation states under alkaline buffers.

Bergmann and co-workers (2015) studied the crystalline Co-oxide Co_3O_4 spinel.[85] This Co_3O_4 catalyst has been widely explored as an active OER catalyst and shares structural motifs with Nocera's CoCat as it consists of Co-deficient CoO_6 layers, which are connected *via* octahedral Co^{3+} ions and tetrahedral Co^{2+} ions.[57,85] Bergmann and co-workers used *in situ* Co K-edge XAS to study the structural changes of the electrocatalyst during OER (Fig. 22). XANES studies indicated a mean oxidation state between 2+ and 3+ for the as-prepared catalyst, consistent with Co_3O_4, whereas upon increasing the electrode potential to OER conditions (+1.62 V *vs.* RHE) the mean oxidation state increased, indicating a higher amount of Co^{3+} and Co^{4+} ions. EXAFS identified changes in the Co coordination during OER, where the OER-active state at +1.62 V *vs.* RHE contained more di-μ-oxo bridged octahedrally coordinated Co ions. After OER, both the XANES and EXAFS structures showed high similarities with the as-prepared catalyst, suggesting that the structural changes were reversible. The geometry of the Co_3O_4 catalyst was also studied by Wang and co-workers (2016).[86] To investigate the active species in the catalyst, *in situ* Co K-edge XAS was used to compare the structure of the Co_3O_4 catalyst to various model catalysts where the tetrahedral Co^{2+} ions or octahedral Co^{3+} ions were substituted with inactive ions. The *in situ* XAS studies with a voltage range of 0.5 to 1.0 V suggested that the tetrahedral Co^{2+}, which is capable of releasing electrons under applied bias, is responsible for the formation of the active CoOOH species.

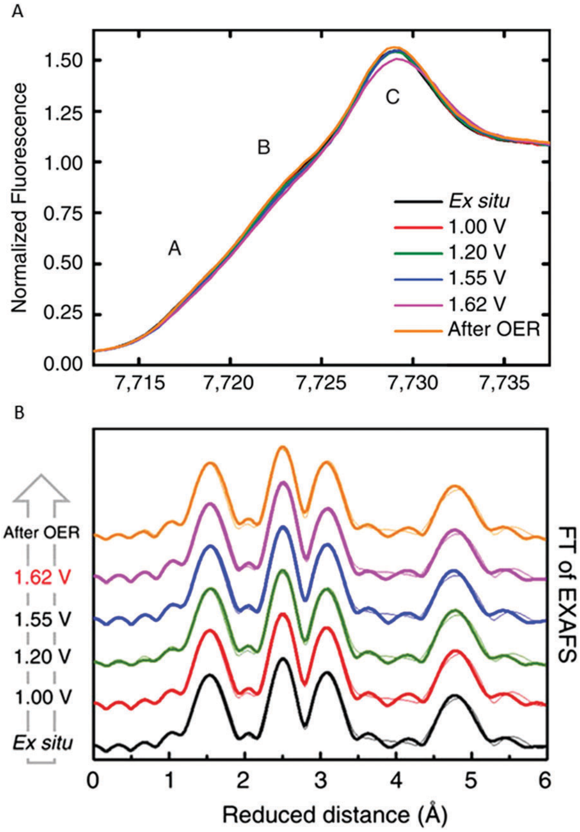

Fig. 22 (A) *In situ* XANES structure of the Co_3O_4 spinel catalyst. (B) *In situ* EXAFS structure of the Co_3O_4 spinel catalyst. Reproduced with permission from ref. 85 under a Creative Commons License CC-BY 4.0.

In situ Co K-edge XAS was used by Seo *et al.* (2016) to study the structure of cobalt oxide nanoparticles of different sizes supported on carbon nanotubes.[87] XANES spectra of the CoO_x catalyst at OCV and OER potential (1.8 V *vs.* RHE) indicated that regardless of the CoO_x particle size, the average oxidation state of Co increased upon increasing the potential to the OER potential. Furthermore, XANES analysis using linear combination fitting and EXAFS studies indicated a phase transformation of Co_3O_4 and/or CoO for the as-prepared catalyst to a Co_3O_4 mixed phase in the active catalyst in OER. By combining the electronic and structural information obtained by the *in situ* XAS experiments with electrocatalytic activity trends it was suggested that Co^{3+} species are related to the active intermediates for OER.

4.2 Nickel-based WOCs

In 2012 Bediako *et al.* studied the electronic and atomic structure in electro-oxidative activated and non-activated NiB$_i$-NiCats using *in situ* XAS.[88] During the electro-oxidative activation the catalyst was held at a potential of 1.1 V in a 1 M KB$_i$ electrolyte (pH = 9.2) for 2.5 hours and an activity increase of three orders of magnitude was observed when compared to a non-activated NiB$_i$-Cat. This contrasts with the CoCats, where high WOC is observed directly upon electro-deposition. Ni K-edge XANES structures were collected for both samples at a potential below the onset for water oxidation catalysis (0.4 V) and at a potential at which oxygen evolution catalysis occurs (1.0 V). At the potential of 0.4 V, nickel centers are found to be in a 2+ oxidation state for both the activated and non-activated catalyst. This oxidation state is lower than that observed in the *ex situ* experiments by Risch and co-workers,[70] which can be explained by reduction due to the applied potential (0.4 V). During water oxidation at a potential of 1.0 V, the non-activated

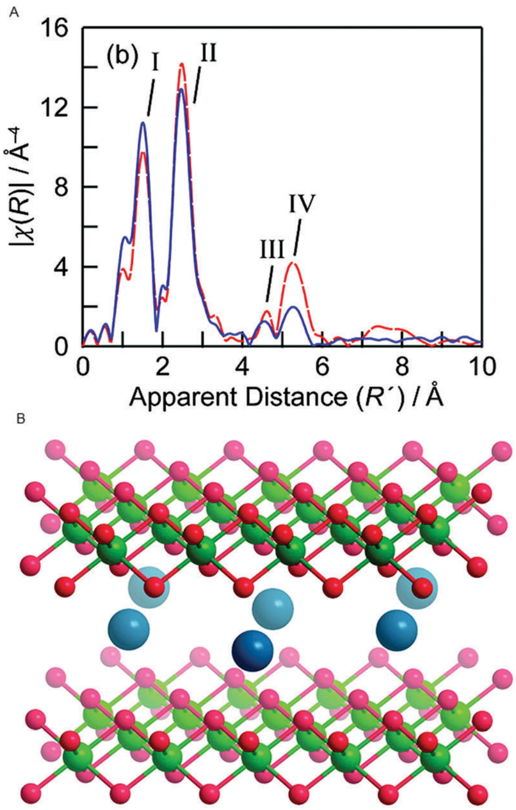

Fig. 23 (A) FT EXAFS structures for a γ-NiOOH reference and the Ni-B_i-cat electro-oxidized at 1.05 V. (B) Crystal structure of γ-NiOOH, with nickel in green, oxygen in red and sodium ion in blue. Water molecules intercalated between the NiO_2 slabs are omitted for clarity. Reprinted with permission from ref. 88. Copyright 2012 American Chemical Society.

Ni-B_i exhibits an oxidation state of 3.16+, whereas the activated Ni-B_i exhibits a mean oxidation state of 3.6+. This indicates that the electro-oxidative pretreatment causes an increase in the presence of Ni 4+ species by a factor of ∼3. The oxidation state of the activated Ni-B_i closely resembles that of the Ni-B_i in the *ex situ* state,[70] suggesting that major changes are predominantly due to the electro-oxidative pretreatment of the catalyst rather than due to reaction conditions.

EXAFS was used to study the local geometry of the Ni centers (Fig. 23). The FT EXAFS of the activated NiCat indicated a Ni–O distance of 1.88 Å and a Ni–Ni distance of 2.82 Å, consistent with a γ-NiOOH structure and the structure reported by *ex situ* XAS studies by Risch *et al.* (2011).[70] The non-activated catalyst showed a EXAFS structure more similar to the Jahn–Teller distorted β-NiOOH, with a Ni–O distance of 1.87 Å and a Ni–Ni distance of 2.03 Å. The oxidation state of 3.16+ found for the non-activated catalyst was consistent with a β-NiOOH phase, whereas the 3.6+ oxidation state found for the activated catalyst was consistent with a γ-NiOOH phase.

Both the change in oxidation state and structure upon electro-oxidative activation suggest a transition from a β-NiOOH phase to a γ-NiOOH phase with a higher amount of Ni^{4+} species. The significantly higher water oxidation activity for electro-oxidative activated NiB_i-cats suggests that γ-NiOOH can be related to a higher OER activity, challenging previous findings where the β-NiOOH phase was found to be more active in OER.[89,90] Reaction conditions do not seem to change the oxidation state of the activated catalyst, either at 1.1 V or 1.15 V, where the OER activity is significantly higher. This suggests that either the transition metal oxide radical generated by hole injection traps the positive charge on the oxygen rather than on the nickel, in the form of an oxyl radical, or a minor equilibrium is established where Ni^{4+} catalytic intermediates formed on applying potential are quickly reduced by water oxidation.

A study on Ni-B_i by Yoshida *et al.* (2014) used *in situ* XAS experiments to study electronic and structural changes.[91] The transformation to a γ-NiOOH species upon applying potential was consistent with the findings of Bediako *et al.* (2012) for their activated Ni-B_i-Cat. During the *in situ* experiment the electrode potential was increased from 0.2 V to 1.1 V, a potential above the onset for water oxidation. XANES analysis indicated the Ni species oxidized from 2.1+ to 3.8+ when going from 0.2 V to 1.1 V. The change in the local structure upon applying a potential was studied by EXAFS. At 0.2 V the local structure of Ni-B_i was in agreement with that of a $Ni(OH)_2$ reference, whereas at 1.1 V, the structure was similar to that of γ-NiOOH.

4.3 Manganese-based WOCs

The active phases of a MnO_x/Au-Si_3N_4 catalyst under electrochemical reaction conditions for OER were studied by Gorlin *et al.* (2013) using *in situ* XAS.[80] Fig. 24A shows the Mn K-edge XANES structures collected at a potential below the onset for water oxidation catalysis (−0.76 V) and at a potential at which

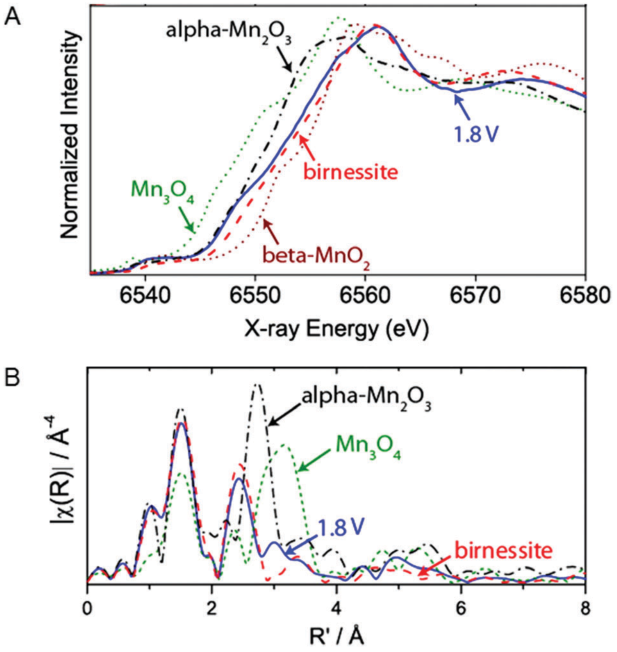

Fig. 24 (A) *In situ* XANES structure of MnO_x/Au-Si_3N_4 film at 1.04 V together with reference spectra of α-Mn_2O_3, β-MnO_2, Mn_3O_4 and birnessite. (B) EXAFS structure of MnO_x/Au-Si_3N_4 film at 1.04 V compared to reference spectra of α-Mn_2O_3, Mn_3O_4 and birnessite. Reprinted with permission from ref. 80. Copyright 2013 American Chemical Society.

oxygen evolution catalysis occurs (1.04 V). When increasing the voltage from −0.76 V to +1.04 V, the oxidation state showed a change from 2.8+ to 3.6+. The oxidation state of 3.6+ is higher than the 3+ oxidation state obtained in the phases of MnO_x explored in the *ex situ* studies. While those phases were grown on different substrates, the comparison indicates that OER conditions lead to a higher Mn oxidation state in MnO_x. The XANES structure of the catalyst under OER conditions showed a strong overlap with the spectrum of birnessite. However, the oxidation state of the MnO_x catalyst was slightly lower than that of a birnessite standard, attributed to the contribution of some electrochemically isolated $Mn_3^{(II,III,III)}O_4$ domains.

The EXAFS structure of the catalyst at −0.76 V indicated a $Mn_3{}^{II,III,III}O_4$ phase. A shift to OER conditions (1.04 V) indicated a structural change to a birnessite-like phase, as shown in Fig. 24B, and therefore bears similarity to the MnO_x catalyst discussed above. However, a smaller coordination number *N* was found, implying a smaller particle size compared to the extended crystalline reference material or the presence of an increased amount of Mn^{2+}.

Yoshida *et al.* (2013) used *in situ* XANES to study the photogenerated carrier transfer towards a Mn oxide cocatalyst on a n-type $Nb:SrTiO_3$ photo-electrode.[92] First the sample was studied as a function of applied potential without UV irradiation. Mn K-edge spectra were measured at several potentials between −1.3 V and +1.7 V. At a potential of −1.3 V a Mn oxidation state of 3+ was found. Upon increasing the potential from −1.3 V to −0.3 V the edge position shifted to higher energy, indicating the partial oxidation of Mn to an oxidation state higher than 3+. The oxidation of Mn upon increasing the potential on $Nb:SrTiO_3$ implies that, under positive applied potential, holes within the $Nb:SrTiO_3$ substrate migrate into the Mn oxide cocatalyst and electrons from the Mn oxide cocatalyst can migrate into the substrate. Upon further increase of the potential to +1.7 V, the edge position remains constant, which could be due to the steady state conditions that do not allow for an accumulation of holes in the Mn oxide cocatalyst.

Upon UV illumination of the Mn oxide cocatalyst at a constant potential of 1.2 V, a gradual shift of the edge energy suggested the oxidation of $Mn^{2.8+}$ to $Mn^{3.6+}$ as shown in Fig. 25A. This oxidation implies the migration of photo-excited holes from the $Nb:SrTiO_3$ substrate to the Mn oxide cocatalyst. Similarly to the voltage dependent experiments, the oxidation state of Mn in a MnO_x compound was found to increase to 3.6+. Another study by Yoshida *et al.* (2014) confirmed the oxidation of Mn^{3+} species to Mn^{4+} species in a Mn oxide cocatalyst on a $SrTiO_3$ photo-electrode during UV irradiation at +0.5 V.[93]

Besides Mn oxide thin films, Mn oxide particles on a $Nb:SrTiO_3$ photo-anode were also studied at 1.2 V under UV illumination (Fig. 25B). The formation of a lower energy peak upon photo-irradiation indicated an increased amount of Mn^{2+}. This suggests that part of the Mn^{3+} reduces to Mn^{2+}, whereas the other part of the Mn oxide particles oxidizes to Mn^{4+} or remains as Mn^{3+}. As Mn^{3+} and Mn^{4+} are believed to function as water oxidation catalysts, both active and inactive Mn oxide was present in the Mn oxide particles.

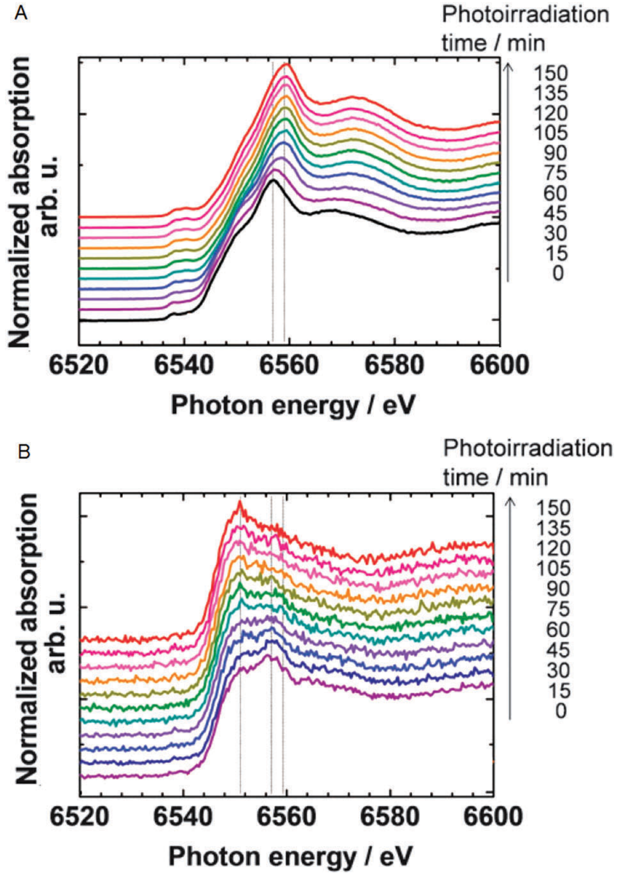

Fig. 25 *In situ* Mn K-edge spectra of the MnO_x (A) thin film and (B) particles on a $Nb:SrTiO_3$ photoelectrode at +1.2 V *vs.* NHE under UV irradiation. Reproduced from ref. 92 with permission from the Royal Society of Chemistry.

For the Mn oxide cocatalyst on a n-type $Nb:SrTiO_3$ photo-electrode, the importance of band bending for the photo-excited hole migration into the catalyst was studied by Mn K-edge XANES experiments under UV irradiation at −0.5 V, 0.0 V and +0.5 V.[93] The XANES structures obtained at both 0.0 V and +0.5 V showed an increase in edge energy, consistent with the oxidation of Mn^{3+} species to Mn^{4+} species. The oxidation state change for the catalyst at 0.0 V was less rapid than that observed for the sample at 0.5 V. The XANES structures at −0.5 V did not show a change in Mn oxidation state under UV irradiation, indicating that photo-excited holes were not transferred to the Mn oxide cocatalyst. The potential-dependence of Mn oxidation for potentials that can significantly alter the band bending, but not the water oxidation activity, suggests that the XAS Mn K-edge measurements report on hole injection driven by band bending in the n-type $Nb:SrTiO_3$ photo-electrode.

4.4 Overview of *in situ* metal K-edge XAS

The *in situ* XAS studies demonstrate the value of *in situ* K-edge XAS in investigating changes in the oxidation state and local environment in WOC materials with applied potential or light. The results are reported in Table 3. For all the studied catalysts it was found that upon increasing the potential to an OER relevant potential, the metal oxidation state increased to a value higher than 3+. This suggests that an increased amount of 4+ species can be important for WOC with Co-, Ni- and Mn-based oxide catalysts. The increased metal oxidation state is a property of either the as-prepared catalyst or the catalyst under reactions, which can be differentiated by comparing *in situ* XAS results to *ex situ* XAS. In the Mn and Co based oxide catalysts, an oxidation state higher than that found in the *ex situ* studies was found. The most clear evidence for a higher oxidation state of the metal under reaction conditions is the increased Co oxidation state for the CoP$_i$-Cats (>3+). The oxidation state of Mn in MnO$_x$ birnessite-like catalysts was found to increase under reaction conditions in two separate studies (one potential, one light driven) to 3.6+ from the nominal value of 3+ observed for the as-prepared catalyst under *ex situ* conditions. It is important to note that the comparison to as-prepared (3+) conditions for MnO$_x$ involves a study by a separate group and on a different substrate. The higher metal oxidation states found for the Co and Mn WOCs under reaction conditions suggest that a transition metal oxide radical with significant metal character is formed. In contrast, the oxidation state of the activated Ni-B$_i$-Cats under reaction conditions closely resembles that of the Ni-B$_i$ in the *ex situ* state,[70] suggesting that major changes are predominantly due to the electro-oxidative pretreatment of the prepared catalyst rather than due to reaction conditions. It is suggested that in Ni oxide catalysts, a radical with oxyl character is created. However, the lack of an oxidation state on the metal site could also be due a rapid pre-equilibrium of Ni 4+ with the solution, or due to the effects of impurities, such as Fe on Ni oxide catalysts.[7] XAS studies of the O K-edge would be helpful in resolving this issue, and are discussed further below.

The *in situ* XAS studies also demonstrate that a reductive potential partially reduces the metal oxidation state. As shown in Table 3, for potentials below the onset for WOC, the metal oxidation state is often lower than the value reported for *ex situ* experiments. This was especially clear for the NiB$_i$-Cats, where an oxidation state of $\sim$2+ was found at potentials of 0.4 V or 0.2 V, significantly lower than the oxidation state observed for a similar catalyst in *ex situ* XAS experiments (>3+).[70] Furthermore, Kanan (2010) found that when the CoP$_i$ system was switched from 1.25 V to OCP, residual water oxidation activity led to a reduction of Co. In the NiB$_i$-Cats, the significant change in the metal oxidation state suggests that the reduction is occurring for bulk Ni centers. On the other hand, a reduction due to residual water oxidation activity in the CoP$_i$ system suggests that surface reactive metals are being reduced. The difference is indicative of a larger role of the metal within the transition metal oxide radical in the Co based catalysts compared to the Ni based catalysts.

As shown by Yoshida and co-workers (2013, 2014), the metal oxidation state can also increase as a result of photo-excited holes. They used XAS to study photo-excited hole transfer into a MnO$_x$ overlayer from a UV-irradiated Nb:SrTiO$_3$ substrate. The fact the Mn oxidation state increased with applied voltage[92,93] indicates that band bending at the MnO$_x$/Nb:SrTiO$_3$ acts as a driving force for photo-excited carrier separation and hole transfer to the catalyst. Studies such as this one by Yoshida suggest that light driven catalysis can be investigated on otherwise "dark" Mn, Co, and Ni catalysts.

EXAFS studies were used to study the structure of the catalyst under OER conditions, also reported in Table 3. In all cases, the structure observed is similar to that found for the as-prepared catalysts studied under *ex situ* conditions. Both Friebel (2013) and Kanan (2010) found a H$_x$CoO$_2$ structure consisting of edge-sharing CoO$_6$ octahedra for the active CoP$_i$-Cats, consistent with the findings by Risch (2009, 2012) in the *ex situ* XAS experiments.[59,83,84] EXAFS studies on the NiCat by Bediako (2012) and Yoshida (2014) suggested a γ-NiOOH species as the active phase, thereby contradicting earlier findings that claimed a β-NiOOH phase to be a more efficient water oxidation catalyst.[88,91] Gorlin and coworkers (2013) found that the active MnO$_x$/Au-Si$_3$N$_4$ catalyst consisted of an oxidized birnessite-like phase, containing Mn^{3+} and Mn^{4+}, and areas with more reduced Mn$_3^{II,III,III}$O$_4$.[80]

5 Other X-ray experiments on WOCs

In this section we describe soft X-ray absorption experiments based on the oxygen K-edge and the metal L-edges of WOCs. Furthermore soft and hard X-ray RIXS experiments will be described. We start with a description of dedicated *in situ* cells for experiments with soft X-rays.

5.1 Development of *in situ* cells

In order to conduct soft X-ray and RIXS experiments under reaction conditions, novel cells had to be designed and developed. While they are reviewed more extensively elsewhere,[94] we provide a brief overview here. From the perspective of the X-ray beam, the cell design is tailored to meet the requirements of a much larger soft X-ray cross section of materials and electrolyte compared to the hard X-ray cross-section (a penetration depth of 100–500 nm for the soft X-ray regime compared with 100s of microns for the hard X-ray regime). The cell also must accommodate a liquid environment near the electrode that is enclosed from the ultra high vacuum (UHV) chamber through which the X-ray beam passes. As opposed to hard X-ray chambers that are completely enclosed by hutches, the soft X-ray beam is on the main floor of the synchrotron and is instead shielded by UHV conditions. Given the large cross section of soft X-rays, along with the long collection times associated with RIXS, the cells are also designed to prevent X-ray induced damage. In particular, they accommodate a flow of the electrolyte to help maintain a similar surface during the course of experiments. These flow conditions also help maintain a similar surface from the perspective of the catalysis itself, which can lead to modifications over time if the electrolyte is not replenished. From the perspective of experimental controls, these flow conditions allow for pH and chemical composition of the electrolyte to be tuned during the course of data collection.

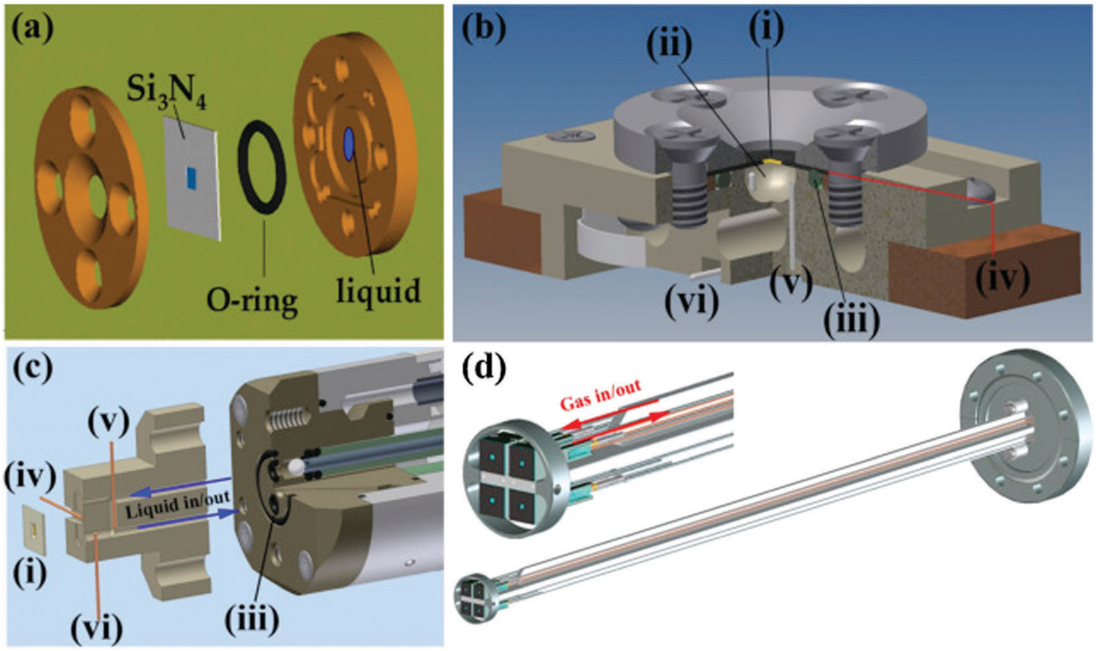

Fig. 26 Cell designs for soft X-ray experiments: (a) static liquid cell, (b) static liquid cell with a 3-electrode setup, (c) a liquid flow cell with a 3-electrode setup, and (d) a gas flow cell. Reprinted with permission from ref. 94, copyright 2015 and ref. 102, copyright 2010 and ref. 103, copyright 2007.

The cell designs, developed largely at the Advanced Light Source at Lawrence Berkeley National Laboratory, are depicted in Fig. 26. Fig. 26(a) shows the essential feature of the cell that allows for it to be accommodated within UHV conditions: namely the transparent window through which the soft X-ray beam passes to the electrode is a 1 × 1 mm, 100 nm thick Si_3N_4 cell window. This cell window, along with an O-ring, effectively seals the liquid from the UHV environment, but is thin enough to be transparent in the soft X-ray regime. A cell containing this cell window can also incorporate the full 3 electrodes necessary for electrochemistry, and a diagram of such a cell is depicted in Fig. 26(b) with (i) denoting the cell window and (ii) the liquid reservoir. The liquid flow cell, depicted in Fig. 26(c), includes the same structure as Fig. 26(b), with the Si_3N_4 cell window (i), the O-ring (iii), and the 3 electrodes (iv, v, and vi), but with an arm that allows for an inlet and outlet of flow to refresh the reservoir. Besides the work at the Advanced Light Source, development and applications of *in situ* soft X-ray transmission liquid cells suitable for following electrochemical reactions were also reported by Kosugi *et al.*[95,96] and Kondoh *et al.*[97,98] While not the focus of this review, gas-phase studies of catalytic surfaces can yield valuable information and a gas flow-cell diagram is shown in Fig. 26(d). In the gas phase, certain experiments such as X-ray photoemission spectroscopy become possible and are more surface sensitive than X-ray absorption. On the other hand, gas-phase studies do not lend themselves to reaction conditions tuned by voltage.

Finally, a range of nanoreactors have been designed especially for use with X-ray microscopes.[99,100] These nanoreactors are used in transmission mode and use two 10–30 nm thin Si_3N_4 windows that hold a 10–100 micron thick gas volume up to pressures of 5 bar. De Smit *et al.* have used such nanoreactors to track simultaneously the metal L edges, the oxygen K edge of the support and the carbon K edge of the substrate and reactants.[101] A similar, modified nanoreactor could also be used for the tracking of water oxidation catalysts under reaction conditions.

5.2 Soft X-ray investigations: O K-edge, M L-edge and RIXS

Although not as exhaustive a list as K-edge and L-edge XAS, various studies have applied oxygen K-edge XAS to explore the effect of the nature of the 3d valence states on catalytic activity. Sun and co-workers (2012) reported the use of O K-edge XAS to study the Ni–O covalence in a NiO_x functionalized silicon WOC and found a more ionic Ni–O bonding.[72] Yoshida *et al.* (2015) reported an *in situ* XAS study on the O K-edge of the Ni-B_i catalyst.[98] By monitoring the oxygen species in the Ni-B_i thin film, the formation of NiO_6 octahedral domains could be directly monitored. Different behaviour for upward and downward potential sweeps suggested that the water oxidation catalysis likely proceeds at the domain edge of the NiO_6 octahedra. More recently, based on the results obtained from a combination of XAS and RIXS, Xiao *et al.* suggested that enhancement in water oxidation catalytic activity originated from a narrowing of the local HOMO–LUMO gap when potential and visible light illumination were simultaneously applied to a dinuclear Mn^{3+} system.[104] RIXS experiments were also performed by Khan and coworkers (2014) on MnO_x nanoparticles loaded into Nafion, indicating that the MnO_x catalyst with the lowest d–d transitions and the strongest charge transfer showed the highest catalytic activity.[81] Bokarev *et al.* studied the difference in the behaviour of the different oxidation states of manganese regarding the photo-electrooxidation of water.[105]

5.3 Hard X-ray RIXS

Friebel *et al.* combined 1s XAS with 1s2p (Kα) RIXS in order to identify the active state of a Co electrocatalyst during the oxygen evolution reaction.[84] They showed the 1s2p RIXS planes of cobalt oxides, where CoO has multiple pre-edge quadrupole-based peaks due to the coupled 1s3d excitation and 1s2p decay, as calculated by Kurian *et al.*[43] The 1s2p RIXS plane of trivalent oxides looks quite different and is dominated by the non-local dipole peak due to 1s4p dipole transitions into the 3d-band.[106] Using these references, a gold-supported cobalt oxide was tracked during oxygen formation.[84] Glatzel and co-workers highlighted the advantage of RIXS analysis on the Mn K pre-edge feature for a series of Mn model complexes to access detailed spin features.[107]

6 Conclusions

As the search for a viable water oxidation catalyst for incorporation into a large scale solar fuel device progresses, the fundamental understanding of the structure–activity relationship needs to be explored and XAS is a strong characterization tool that provides valuable insight. Thus far, some of the most catalytically active WOCs – namely Co, Ni, and Mn oxides – have shown similar, as-prepared electronic structures with an average metal oxidation state of 3+, octahedral coordination, and a M–O distance of ∼1.9 Å. The M–M distance of ∼2.8 Å suggests the importance of di-μ oxo bridging between neighboring metal sites, which bears similarity to the Mn–oxide complex of photosystem II. For the Mn and Co oxide catalysts, the metal oxidation state increases (>3+) under reaction conditions, suggesting that the transition metal oxide radical has significant metal character. In contrast, the metal oxidation state of Ni oxide catalysts is not observed to change under reaction conditions. In all cases studied thus far, the coordination environment of the catalyst does not change under reaction conditions, at the level of XAS and EXAFS sensitivity to the structure. In general, EXAFS finds that M–M distances beyond nearest neighbor are significantly suppressed in the more active WOCs, which suggests that disorder is correlated with activity. Further correlations with activity were explored using the well-defined, homogeneous structures of the Co-POMs. However, XAS and EXAFS could not differentiate catalysts with similar overall electronic structures, but with significant differences in activity. The X-ray studies of heterogeneous and homogeneous WOCs would significantly benefit from X-ray techniques that are more sensitive to the electronic structure, in order to determine to what extent the metal and oxygen are involved in the transition metal oxide radical and to differentiate details in the ground state electronic structure that could be markers of activity. Therefore, two further directions are proposed: (1) soft X-ray O K-edge XAS studies of as-prepared catalysts and under reaction conditions and (2) RIXS studies of the ground state electronic structure, focused on d–d transitions and charge transfer between metal and oxygen sites.

References

1 F. Osterloh and B. Parkinson, *MRS Bull.*, 2011, **36**, 17–22.
2 A. Ismail and D. Bahnemann, *Sol. Energy Mater. Sol. Cells*, 2014, **128**, 85–101.
3 R. Eisenberg and H. Gray, *Inorg. Chem.*, 2008, **47**, 1697–1699.
4 G. Ketteler, S. Yamamoto, H. Bluhm, K. Andersson, D. Starr, D. Ogletree, H. Ogasawara, A. Nilsson and M. Salmeron, *J. Phys. Chem. C*, 2007, **111**, 8278–8282.
5 M. Zhang and H. Frei, *Catal. Lett.*, 2015, **145**, 420.
6 J. Guo, P. Glans, Y. Liu and C. Chang, *On Solar Hydrogen and Technology, Electronic Structure Study of Nanostructured Transition Metal Oxides Using Soft X-Ray Spectroscopy*, John Wiley and Sons, Asia, 1st edn, 2009.
7 M. S. Burke, L. J. Enman, A. S. Batchellor, S. Zou and S. W. Boettcher, *Chem. Mater.*, 2015, **27**, 7549–7558.
8 M. Zhang, M. de Respinis and H. Frei, *Nat. Chem.*, 2014, **6**, 362–367.
9 F. L. Formal, E. Pastor, S. Tilley, C. Mesa, S. Pendlebury, M. Grätzel and J. Durrant, *J. Am. Chem. Soc.*, 2015, **137**, 6629–6637.
10 O. Zandi and T. W. Hamann, *Phys. Chem. Chem. Phys.*, 2015, **17**, 22485–22503.
11 J. Guo, *Int. J. Quantum Chem.*, 2009, **109**, 2714–2721.
12 R. Hocking, R. Brimblecombe, L. Chang, A. Singh, M. Cheah, C. Glover, W. Casey and L. Spiccia, *Nat. Chem.*, 2011, **3**, 461–466.
13 E. Miller and R. Rocheleau, *J. Electrochem. Soc.*, 1997, **144**, 1995–2003.
14 V. Artero, M. Chavarot-Kerlidou and M. Fontecave, *Angew. Chem., Int. Ed.*, 2011, **50**, 7238–7266.
15 E. Fabbri, A. Habereder, K. Waltar, R. Kötz and T. Schmidt, *Catal. Sci. Technol.*, 2014, **4**, 3800–3821.
16 S. Lee, D. González-Flores, J. Ohms, T. Trost, H. Dau, I. Zaharieva and P. Kurz, *ChemSusChem*, 2014, **7**, 3442–3451.
17 P. Rasiyah and A. Tseung, *J. Electrochem. Soc.*, 1984, **131**, 803.
18 S. Trasatti, *J. Electroanal. Chem.*, 1980, **111**, 125.
19 Y. Surendranath, M. Kanan and D. Nocera, *J. Am. Chem. Soc.*, 2010, **132**, 16501.
20 D. Bediako, Y. Surendranath and D. Nocera, *J. Am. Chem. Soc.*, 2013, **135**, 3662.
21 D. Bediako, C. Costentin, E. Jones, D. Nocera and J. Savéant, *J. Am. Chem. Soc.*, 2013, **135**, 3662.
22 M. Huynh, D. Bediako and D. Nocera, *J. Am. Chem. Soc.*, 2014, **136**, 6002.
23 D. Herlihy, M. Waegele, X. Chen, C. Pemmaraju, D. Prendergast and T. Ćuk, *Nat. Chem.*, 2016, **8**, 549–555.
24 O. Zandi and T. Hamann, *Nat. Chem.*, 2016, **8**, 778–783.
25 D. Moonshiram, I. Alperovich, J. Concepcion, T. Meyer and Y. Pushkar, *Proc. Natl. Acad. Sci. U. S. A.*, 2013, **110**, 3765–3770.
26 G. Bunker, *Introduction to XAFS: A Practical Guide to X-ray Absorption Fine Structure*, Cambridge University Press, 2010.
27 J. Stohr, *NEXAFS Spectroscopy*, Springer, 1992.

28 J. Rehr and R. Albers, *Rev. Mod. Phys.*, 2000, **72**, 621–654.

29 F. de Groot and A. Kotani, *Core Level Spectroscopy of Solids*, CRC Press, 1st edn, 2008.

30 A. Kudo and Y. Miseki, *Chem. Soc. Rev.*, 2009, **38**, 253–278.

31 F. Osterloh, *Chem. Soc. Rev.*, 2013, **42**, 2294–2320.

32 H. Ahmad, S. Kamarudin, L. Minggu and M. Kassim, *Renewable Sustainable Energy Rev.*, 2015, **43**, 599–610.

33 X. Deng and H. Tuysuz, *ACS Catal.*, 2014, **4**, 3701–3714.

34 D. Joseph, S. Basu, S. Jha and D. Bhattacharyya, *Nucl. Instrum. Methods Phys. Res., Sect. B*, 2012, **274**, 126–128.

35 J. Wong, F. Lytle, R. Messmer and D. Maylotte, *Phys. Rev. B: Condens. Matter Mater. Phys.*, 1984, **30**, 5596–5610.

36 G. Henderson, F. de Groot and B. Moulton, *Rev. Mineral. Geochem.*, 2014, **78**, 75–138.

37 T. Westre, P. Kennepohl, J. De Witt, B. Hedman, K. Hodgson and E. Solomon, *J. Am. Chem. Soc.*, 1997, **119**, 6297–6314.

38 F. de Groot, G. Vanko and P. Glatzel, *J. Phys.: Condens. Matter*, 2009, **21**, 104207.

39 D. Koningsberger, B. Mojet, G. van Dorssen and D. Ramaker, *Top. Catal.*, 2000, **10**, 143–155.

40 M. Newville, *Fundamentals of XAFS*, 1st edn, 2004, Published online: http://xafs.org/Tutorials.

41 J. Cook Jr. and D. Sayers, *J. Appl. Phys.*, 1981, **52**, 5024–5031.

42 L. Ament, M. van Veenendaal, T. Devereaux, J. Hill and J. van den Brink, *Rev. Mod. Phys.*, 2011, **83**, 705–767.

43 R. Kurian, M. van Schooneveld, N. Zoltan, G. Vankó and F. de Groot, *J. Phys. Chem. C*, 2013, **117**, 2972–2981.

44 A. Juhin, F. de Groot, G. Vankó, M. Calandra and C. Brouder, *Phys. Rev. B: Condens. Matter Mater. Phys.*, 2010, **81**, 115115.

45 A. Singh, S. Chang, R. Hocking, U. Bach and L. Spiccia, *Energy Environ. Sci.*, 2013, **6**, 579–586.

46 C. Ohlin, S. Harley, J. McAlpin, R. Hocking, B. Mercado, R. Johnson, E. Villa, M. Fidler, M. Olmstead, L. Spiccia, R. Britt and W. Casey, *Chem. – Eur. J.*, 2011, **17**, 4408–4417.

47 D. M. Robinson, Y. B. Go, M. Mui, G. Gardner, Z. J. Zhang, D. Mastrogiovanni, E. Garfunkel, J. Li, M. Greenblatt and G. C. Dismukes, *J. Am. Chem. Soc.*, 2013, **135**, 3494–3501.

48 I. Zaharieva, P. Chernev, M. Risch, K. Klingan, M. Kohlhoff, A. Fischer and H. Dau, *Energy Environ. Sci.*, 2012, **5**, 7081–7089.

49 B. Thole and G. van der Laan, *Phys. Rev. B: Condens. Matter Mater. Phys.*, 1988, **38**, 3158–3171.

50 F. Morales, F. de Groot, P. Glatzel, E. Kleimenov, H. Bluhm, M. Havecker, A. Knop-Gericke and B. Weckhuysen, *J. Phys. Chem. B*, 2004, **108**, 16201–16207.

51 M. Delgado-Jaime and P. Kennepohl, *J. Synchrotron Radiat.*, 2010, **17**, 119–128.

52 J. Suntivich, W. Hong, Y. Lee, J. Rondinelli, W. Yang, J. Goodenough, B. Dabrowski, J. Freeland and Y. Shao-Horn, *J. Phys. Chem.*, 2014, **118**, 1856–1863.

53 J. Suntivich, H. Gasteiger, N. Yabuuchi, H. Nakanishi, J. Goodenough and Y. Shao-Horn, *Nat. Chem.*, 2011, **3**, 546–550.

54 J. Suntivich, K. May, H. Gasteiger, J. Goodenough and Y. Shao-Horn, *Science*, 2011, **334**, 1383–1385.

55 F. de Groot, M. Grioni, J. Fuggle, J. Ghijsen, G. Sawatzky and H. Petersen, *Phys. Rev. B: Condens. Matter Mater. Phys.*, 1989, **40**, 5715–5723.

56 E. Solomon, B. Hedman, K. Hodgson, A. Dey and R. Szilagyi, *Coord. Chem. Rev.*, 2005, **249**, 97–129.

57 M. Kanan and D. Nocera, *Science*, 2008, **321**, 1072–1075.

58 M. Risch, V. Khare, I. Zaharieva, L. Gerencser, P. Chernev and H. Dau, *J. Am. Chem. Soc.*, 2009, **131**, 6936–6937.

59 M. Risch, K. Klingan, F. Ringleb, P. Chernev, I. Zaharieva, A. Fischer and A. Dau, *ChemSusChem*, 2012, **5**, 542–549.

60 Y. Surendranath, M. Dinça and D. Nocera, *J. Am. Chem. Soc.*, 2009, **131**, 2615–2620.

61 H. Dau, P. Liebisch and M. Haumann, *Anal. Bioanal. Chem.*, 2003, **376**, 562–583.

62 T. Yamamoto, *X-Ray Spectrom.*, 2008, **37**, 572–584.

63 A. Sartorel, M. Carraro, G. Scorrano, R. De Zorzi, S. Geremia, N. McDaniel, S. Bernhard and M. Bonchio, *J. Am. Chem. Soc.*, 2008, **15**, 5006–5007.

64 Q. Yin, J. Tan, C. Besson, Y. Geletii, D. Musaev, A. Kuznetsov, Z. Luo, K. Hardcastle and C. Hill, *Science*, 2010, **328**, 342–345.

65 R. Schiwon, K. Klingan, H. Dau and C. Limberg, *Chem. Commun.*, 2014, **50**, 100–102.

66 A. Hibberd, H. Doan, E. Glass, F. de Groot, C. Hill and T. Ćuk, *J. Phys. Chem. C*, 2015, **119**, 4173–4179.

67 H. Lv, J. Song, Y. Geletii, J. Vickers, J. Sumliner, D. Musaev, P. Kögerler, P. Zhuk, J. Bacsa, G. Zhu and C. Hill, *J. Am. Chem. Soc.*, 2014, **136**, 9268–9271.

68 J. Stracke and R. Finke, *J. Am. Chem. Soc.*, 2011, **133**, 14872–14875.

69 M. Dinça, Y. Surendranath and D. Nocera, *Proc. Natl. Acad. Sci. U. S. A.*, 2010, **107**, 10337–10341.

70 M. Risch, K. Klingan, J. Heidkamp, D. Ehrenberg, P. Chernev and I. Zaharieva, *Chem. Commun.*, 2011, **47**, 11912–11914.

71 H. Dau and M. Haumann, *Coord. Chem. Rev.*, 2008, **252**, 273–295.

72 K. Sun, N. Park, Z. Sun, J. Zhou, J. Wang, X. Pang, S. Shen, S. Noh, Y. Jing, S. Jin, P. Yu and D. Wang, *Energy Environ. Sci.*, 2012, **5**, 7872–7877.

73 K. Yachandra, K. Sauer and M. Klein, *Chem. Rev.*, 1996, **96**, 2927–2950.

74 M. Morita, C. Iwakura and H. Tamura, *Electrochim. Acta*, 1977, **22**, 325–328.

75 M. Morita, C. Iwakura and H. Tamura, *Electrochim. Acta*, 1978, **4**, 331–335.

76 T. Takashima, K. Hashimoto and R. Nakamura, *J. Am. Chem. Soc.*, 2012, **134**, 1519–1527.

77 C. Kuo, I. Mosa, A. Poyraz, S. Biswas, A. El-Sawy, W. Song, Z. Luo, S. Chen, J. Rusling, J. He and J. Suih, *ACS Catal*, 2015, **5**, 1693–1699.

78 F. Jiao and H. Frei, *Chem. Commun.*, 2010, **46**, 2920–2922.

79 S. Webb, B. Tebo and J. Bargar, *Am. Mineral.*, 2005, **90**, 1342–1357.

80 Y. Gorlin, B. Lassalle-Kaiser, J. Benck, S. Gul, S. Webb, V. Yachandra, J. Yano and T. Jaramillo, *J. Am. Chem. Soc.*, 2013, **135**, 8525–8534.

81 M. Khan, E. Suljoti, A. Singh, S. Bonke, T. Brandenburg, K. Atak, R. Golnak, L. Spiccia and E. Aziz, *J. Mater. Chem. A*, 2014, **2**, 18199–18203.

82 J. Park, H. Kim, K. Jin, B. Lee, Y.-S. Park, H. Kim, I. Park, K. Yang, H.-Y. Jeong, J. Kim, K. Hong, H. Jang, K. Kang and K. Nam, *J. Am. Chem. Soc.*, 2014, **136**, 4201–4211.

83 M. Kanan, J. Yano, Y. Surendranath, M. Dina, V. Yachandra and D. Nocera, *J. Am. Chem. Soc.*, 2010, **132**, 13692–13701.

84 D. Friebel, M. Bajdich, B. Yeo, M. Louie, D. Miller, H. Casalongue, F. Mbuga, T. Weng, D. Nordlund, D. Sokaras, R. Alonso-Mori, A. T. Bell and A. Nilsson, *Phys. Chem. Chem. Phys.*, 2013, **15**, 17460–17467.

85 A. Bergmann, E. Martinez-Moreno, D. Teschner, P. Chernev, M. Gliech, J. Ferreira de Araújo, T. Reier, H. Dau and P. Strasser, *Nat. Commun.*, 2015, **6**, 8625.

86 H.-Y. Wang, S.-F. Hung, H.-Y. Chen, T.-S. Chan, H. Chen and B. Liu, *J. Am. Chem. Soc.*, 2016, **138**, 36–39.

87 B. Seo, Y. Sa, J. Woo, K. Kwon, J. Park, T. Shin, H. Jeong and S. Joo, *ACS Catal.*, 2016, **6**, 4347–4355.

88 D. Bediako, B. Lassalle-Kaiser, Y. Surendranath, J. Yano, V. Yachandra and D. Nocera, *J. Am. Chem. Soc.*, 2012, **134**, 6801–6809.

89 P. Lu and S. Srinivasan, *J. Electrochem. Soc.*, 1978, **125**, 1416–1422.

90 M. Lyons and M. Brandon, *Int. J. Electrochem. Sci.*, 2008, **3**, 1386–1424.

91 M. Yoshida, T. Iida, T. Mineo, T. Yomogida, K. Nitta, K. Kato, H. Nitani, H. Abe, T. Uruga and H. Kondoh, *Electrochemistry*, 2014, **82**, 355–358.

92 M. Yoshida, T. Yomogida, T. Mineo, K. Nitta, K. Kato, T. Masuda, H. Nitani, H. Abe, S. Takakusagi, T. Uruga, K. Asakura, K. Uosaki and H. Kondoh, *Chem. Commun.*, 2013, **49**, 7848–7850.

93 M. Yoshida, T. Yomogida, T. Mineo, K. Nitta, K. Kato, T. Masuda, H. Nitani, H. Abe, S. Takakusagi, T. Uruga, K. Asakura, K. Uosaki and H. Kondoh, *J. Phys. Chem.*, 2014, **118**, 24302–24309.

94 Y. Liu, P. Glans, C. Chuang, M. Kapilashrami and J. Guo, *J. Electron Spectrosc. Relat. Phenom.*, 2015, **200**, 282–292.

95 M. Nagasaka, T. Hatsui, T. Horigome, Y. Hamamura and N. Kosugi, *J. Electron. Spectrosc. Relat. Phenom.*, 2010, **177**, 130–134.

96 M. Nagasaka, H. Yuzawa and N. Kosugi, *J. Electron. Spectrosc. Relat. Phenom.*, 2015, **200**, 293–310.

97 R. Toyoshima and H. Kondoh, *J. Phys.: Condens. Matter*, 2015, **27**, 083003.

98 M. Yoshida, Y. Mitsutomi, T. Mineo, M. Nagasaka, H. Yuzawa, N. Kosugi and H. Kondoh, *J. Phys. Chem. C*, 2015, **119**, 19279–19286.

99 F. de Groot, E. de Smit, M. van Schooneveld, L. Aramburo and B. Weckhuysen, *ChemPhysChem*, 2010, **11**, 951.

100 S. Kelly, P. Nigge, S. Prakash, A. Laskin and B. Wang, *Rev. Sci. Instrum.*, 2013, **84**, 073708.

101 E. de Smit, I. Swart, J. Creemer, G. Hoveling, M. Gilles, T. Tyliszczak, P. Kooyman, H. Zandbergen, C. Morin, B. Weckhuysen and F. de Groot, *Nature*, 2008, **456**, 222.

102 P. Jiang, J.-L. Chen, F. Borondics, P.-A. Glans, M. West, C.-L. Chang, M. Salmeron and J. Guo, *Electrochem. Commun.*, 2010, **12**, 820–822.

103 J. Guo, T. Tong, L. Svec, J. Go, C. Dong and J.-W. Chiou, *J. Vac. Sci. Technol., A*, 2007, **25**, 1231.

104 J. Xiao, M. Khan, A. Singh, E. Suljoti, L. Spiccia and E. Aziz, *ChemSusChem*, 2015, **8**, 872–877.

105 S. Bokarev, M. Khan, M. Abdel-Latif, J. Xiao, R. Hilal, S. Aziz, E. Aziz and O. Kühn, *J. Phys. Chem. C*, 2015, **119**, 19192–19200.

106 G. Vankó, F. de Groot, S. Huotari, R. Cava, T. Lorenz and M. Reuther, 2008, arXiv:0802.2744.

107 P. Glatzel and U. Bergmann, *Coord. Chem. Rev.*, 2005, **249**, 65–95.